Age Hardening in Transition Metal Aluminium Nitride Thin Films Studied at the Atomic Scale

Doctoral Thesis

Dipl.-Ing. Richard Hans Rachbauer

Department of Physical Metallurgy and Materials Testing
Montanuniversität Leoben

Leoben, July 2011

This work was supported by the Austrian Science Fund
in the framework of START Project Y371.

Affidavit:
I declare in lieu of oath, that I wroth this thesis and performed the associated research myself, using only literature cited in this volume.

Acknowledgements

At this point I want to express my gratefulness to people who endured the last years of scientific discussions with me, arising during and/or after work, as well as over one or the other beer.

First of all, I owe my sincere gratitude to my supervisor **Paul H. Mayrhofer** for his strong support and trust. Your great encouragement and the liberty you granted me for my own ideas are scarcely found in the field we work. Besides your dense schedule, you always had a minute for scientific discussions but additionally about non-work related issues, which left a deep footprint in my perspective on many topics in life.

In line with him, I want to express my personal thanks to **David Holec** for his great efforts in making me understand that a couple of atoms and some electrons in between can provide great insights into materials science. Further, this guardian of our Think-Tank provided many helpful ideas and long discussions on the scope of my work but also way beyond. After three years of cooperation with you both I have to admit, that I am now convinced that scientific "*insbeeration*" has not necessarily to come from Göss but can also stem from wine of your homelands.

I am also grateful to all **my former and present colleagues** within the **Thin Films Group**, but also in the "**Substrate Group**" (High Performance Structural Materials and Testing) at the **Department of Physical Metallurgy and Materials Testing** in Leoben. Thank you all for the vital chats and discussions during work, coffee and especially after work.

Special thanks should be addressed to the **technical staff** in Leoben, foremost to **Gerhard Hawranek** and **Reinhilde Stopar**, for your quick support and helping hands in tricky situations.

I also have to thank my Diploma Students, **Andreas Blutmager**, **Zehua Zhang** and **Lan Wang**, who taught me how to teach and that patience can be a great mercy.

To all **my friends, with and without "Couleur"**, I owe my gratitude for retaining a

strong band of friendship, even in times of seldom encounter.

The last few years also included some funny bits during interviews on the scope of my work. It is to **my family** whom I want to thank and exemplarily show with this thesis what makes the small difference between "*Werkstoff*-" and "*Werkstattwissenschaften*". I am looking forward to celebrate with you the successful proof of this tiny issue.

The most important person in my life must of course be thought of last but not least. It is to **Astrid**, who was the biggest force backing me up. Without complaints you encouraged me to get the things done successfully and my eyes straight looking forward. Without your daily support in every situation of life during the last "almost-decade", it would not have been possible to finish this thesis. My lovely thanks to you, and lets get ready for the next steps in life.

Contents

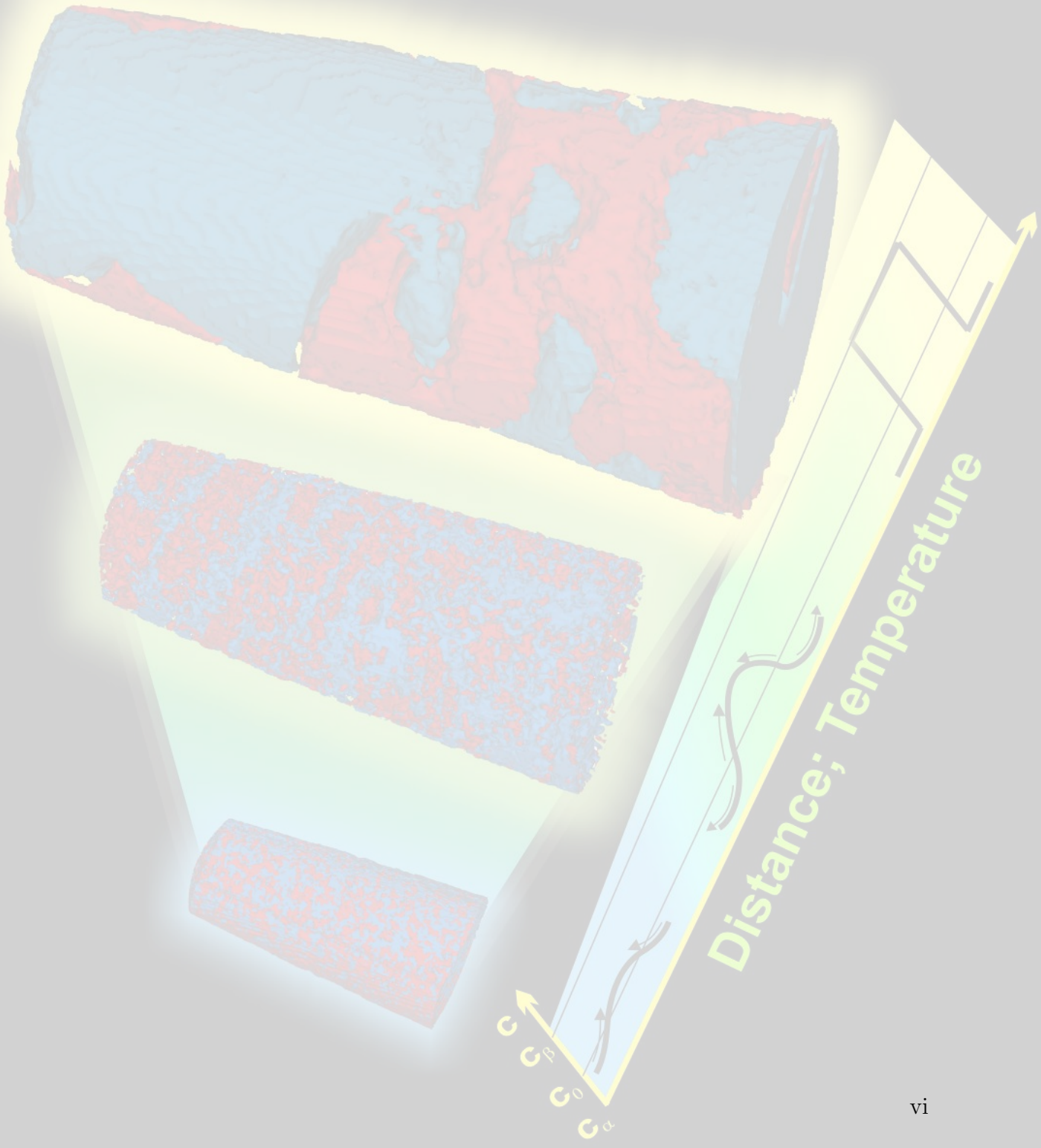

Chapter 1

Introduction

Research and development of modern application tailored materials implements a tremendous need for a detailed understanding of the intrinsic material properties and suitable combinations. An unacquainted person would probably believe that highest purity and single crystallinity of a material yields optimised properties. This perspective however fails in most cases, as many important material properties as e.g. hardness and ductility, or electrical, optical and thermal properties are determined by the incorporation of defects and tremendously depend on their respective length scale. During the last decades a trend in materials design concepts can be observed from the macro-scale engineering level towards the understanding and utilisation of microstructural features. This evolution is nowadays continued towards the nano-scale, where classical engineering concepts are insufficient for a description of the resulting properties [1–3].

State-of-the-art thin film technology benefits from the unique size-dependent properties at the small end of the scale bar, resulting in a huge range of diverse applications from e.g. electronic, optical and medical towards protective devices. Often low coating synthesis temperatures (e.g. plasma-assisted vapour deposition techniques the substrate temperature is below 0.2-0.3 of the melting point in Kelvin) are used [4], which leads to limited ad-atom kinetics during deposition. This enables for the synthesis of coating structures and metastable phases far off the thermodynamic equilibrium. Metastable phases are frequently characterised by stresses or small grain sizes in the nanometer range, which in turn result in extraordinary physical (e.g. superhardness with $H \geq 0\,\mathrm{GPa}$) and thermal (e.g. hardness increase with work load – *age hardening*) properties in comparison to their equilibrium counterparts. Especially in the field of hard protective coatings, the group of transition metal nitrides attracts industrial interest because of their high melting point, high hardness and fairly good oxidation and corrosion resistance [5–7].

The thermal stability of transition metal nitride coatings is thus strongly affected by annealing and consequential recovery (stress relaxation), interdiffusion, recrystallisation, or phase transformation. These phenomena are technologically relevant since the resulting structure (on both micro- and nanoscale) has a large impact on the film properties. Therefore, the development of advanced hard thin films is preferably made using phase transformation concepts from physical metallurgy, such as primary (vapour-to-solid) and secondary (e.g. precipitation) phase transformation. Here, a fundamental understanding of the intrinsic properties of single layer transition metal nitrides becomes inevitable, being the key for materials selection and application tailored coating synthesis with respect to more sophisticated architectures, like nanocomposites or nanolaminates [8].

This thesis thereby concentrates on the development of a state-of-the-art understanding of metastable phases in nitrides and their decomposition processes to reach equilibrium. In order to work out a detailed knowledge of the thermal stability of transition metal nitrides, a major part is devoted to investigations of the coating structure and their physical and thermal properties at the atomic level. A combinatorial approach was chosen, involving theoretical and experimental work, to study the thermally induced isostructural decomposition of $Ti_{1-x}Al_xN$ coatings. The spinodal decomposition of $Ti_{1-x}Al_xN$ hard coatings implements a substantial hardness increase with annealing temperature or time, respectively, commonly referred to as *age hardening*. This particular feature is believed to bear a high potential with respect to the enhancement of tool lifetime, which implements economical but also increasingly environmental considerations. The goal of improving the thermal stability and oxidation resistance is currently approached by the investigation of the alloying effect of transition metals to $Ti_{1-x}Al_xN$. Thereby, density functional theory (DFT) calculations present a well established tool for the prediction of structure and properties of nanometer-sized features, where the properties are determined (or critically influenced) by the electronic structure of the solid [9].

For application tailored materials design it is crucial to acquire basic knowledge on the micro- and nanostructural evolution of the metastable phases as a function of temperature and time. Thus, in Publication I a focused ion beam microscopy (FIB) based specimen preparation technique was modified in order to enable atom probe tomography (APT) of $Ti_{1-x}Al_xN$ thin films. The obtained results are presented in Publications II and III and corroborated by diverse experimental techniques e.g. high resolution transmission electron microscopy (HR-TEM), X-ray diffraction (XRD), or nanoindentation. The alloying effect of group IIIB-VB transition metals (TM) on structure, properties and thermal stability of $Ti_{1-x}Al_xN$ is in the scope of Publications IV to VIII and critically compared to the *ab initio* predicted trends.

As nitrides are nowadays of growing interest in various fields for mechanical as well as many

other functional uses, I am convinced that the above presented research activities provide a valuable support in the field of thin films science and contribute to the development of predictable coating properties.

Chapter 2

Background and Motivation

2.1 Hard Ceramic Materials

Borides, carbides, nitrides, and oxides of transition metal elements (TM) attract industrial and scientific interest for many decades because of their outstanding physical, chemical and thermal properties [10, 11], as e.g. high hardness, wear and corrosion resistance, electrical conductivity and thermal stability. Especially harsh environments resemble a strong driving force for research of hard ceramic structural components, such as seals in contact with corrosive media or crucibles and furnace parts for extremely high temperatures. Among this group of hard materials, especially the introduction of thin film deposition processes considerably extended the technological usage of TM-nitrides (TMN) and -oxides due to enhanced size-dependent properties [1, 12]. Compared to their bulk counterparts, TMN thin films are industrially well acknowledged for their adaptability by means of composition, structure and thus wide range of technological feasibility as protective and functional coatings for tools or electronic devices.

State of the art physical or chemical vapour deposition techniques (PVD, CVD) [13, 14] enable for the synthesis of micro- and nanostructures at conditions far away from the thermodynamic equilibrium. Some crucial parameters, such as temperature and particle energy and their impact on the microstructural evolution during deposition are summarised in Fig. 2.1. Further information on the influence of pressure, bias voltage or impurity content is given in Refs. [15–18].

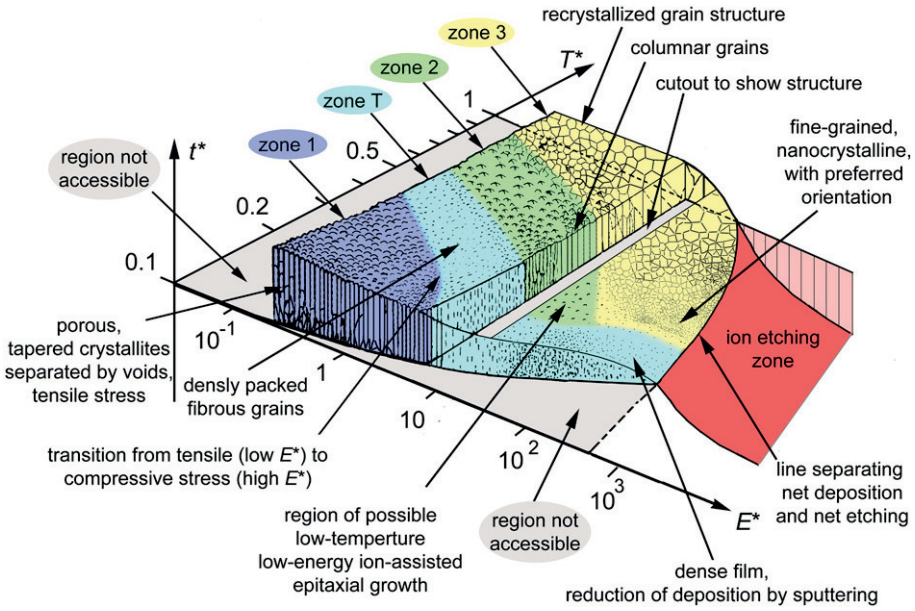

Figure 2.1: Structure zone diagram adapted from Ref. [18]: $T^\star$, $E^\star$, $t^\star$ give the generalised temperature, normalised energy flux and thickness, respectively. The zone boundaries are gradual and for illustration only. Axis coordinates may differ for diverse materials.

2.2 Transition Metal Nitrides

The most prominent representatives for TMN are found within the $4d$ to $6d$ transition metals, e.g. ScN, TiN, VN, CrN, YN, ZrN, NbN or TaN. Their major application as protective coatings on cutting and milling tools is related to their high melting points, hardness and thermal conductivity [19–22]. These criteria make them also attractive for electronic and optical components such as heat sinks or diffusion barriers [23]. In the field of hard materials, the cubic (fcc, B1-structure, $Fm\bar{3}m$ space group, NaCl-prototype) modification, with its six-fold coordination implying short interatomic distances, is favoured over the extensive group of hexagonal crystal structures [7]. The hexagonal five- or four-fold co-ordinations appear in e.g. BN (hex, B_k-structure, $P6_3/mmc$ space group) or AlN (wurtzite, B4-structure, $P6_3mc$ space group, ZnS-prototype), respectively [24]. The number of nearest neighbours is strongly depending on the valence electron configuration of the interacting elements and thus determines the thermodynamically stable phase. Since the incorporation of nitrogen in TMs occurs mostly by an interstitial mechanism, nitrides can be formed in various stoichiometries and crystal structures, as e.g. in the case of Ta_mN_n at least seven allotropes can be identified [25]. Thus the electronic configuration strongly determines the different properties of TMN, which can be attributed to three predominant bonding types (e.g. covalent, metallic or ionic), as exemplarily shown in Fig. 2.2.

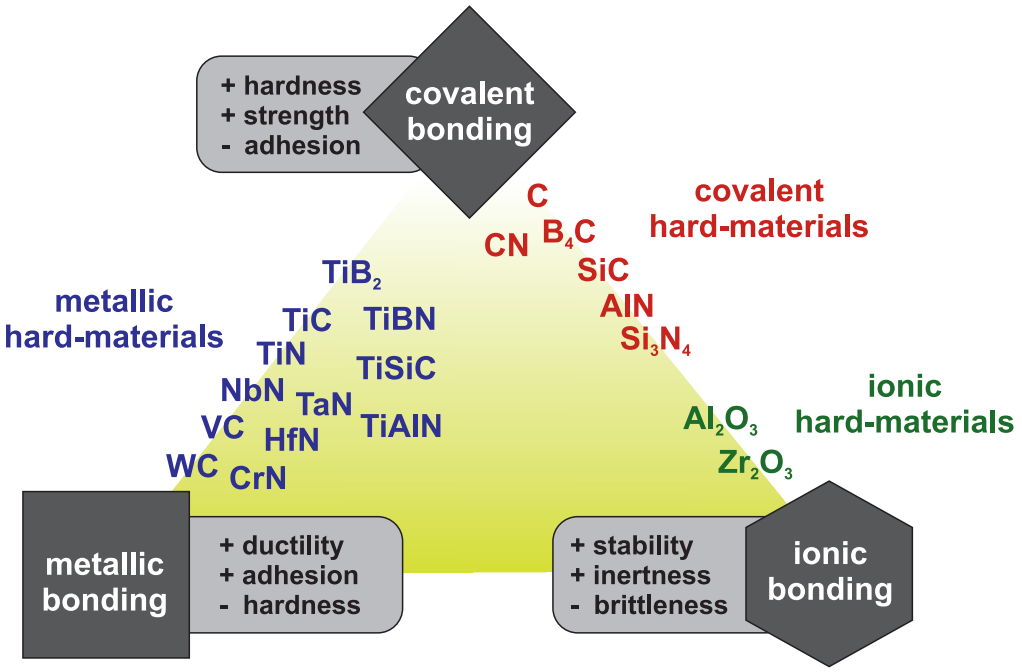

Figure 2.2: Classification of hard ceramic materials according to their chemical bonding and the corresponding change in properties (modified after [10, 26, 27].

By means of density functional theory (DFT) it is possible to access the electronic structure of solids. Due to the deposition conditions at highest cooling rates even structures which do not exhibit the energetic minimum configuration can be realised. In case of complex TMN compounds, ab initio calculations are widely used to predict and understand materials properties and support the development of application tailored materials design [28]. A prediction of the local electron distribution gives rise on the preferred bonding type and enables for the determination of the density of states (DOS). The electron population of states at the different energy levels depends on structure and composition of the respective TMN compound. Thus, it is possible to discriminate between the individual bonding contributions of the interacting N- and TM-electrons, as shown in principal for TiN in Fig. 2.3.

While the core electrons at energies far below the Fermi level, E_F, do not contribute to bonding, the region between ≈ -10 and $\approx -2\,\mathrm{eV}$ can be understood as the bonding states responsible for the covalent character of the compound. The N p-orbitals interact with the TM d-orbitals, forming a so called sp^3d^2-hybridisation, which results in an e_g-symmetry (electron localisation along $\langle 100 \rangle$ directions in Fig. 2.4a) in fcc crystals. The states from $\approx -2\,\mathrm{eV}$ to E_F, referred to as the metallic region, however mainly host Ti d-electrons. Since the TM d-states localised in this region can be regarded less strongly bound compared to the energetically lower bonding states, the corresponding states are understood to mostly

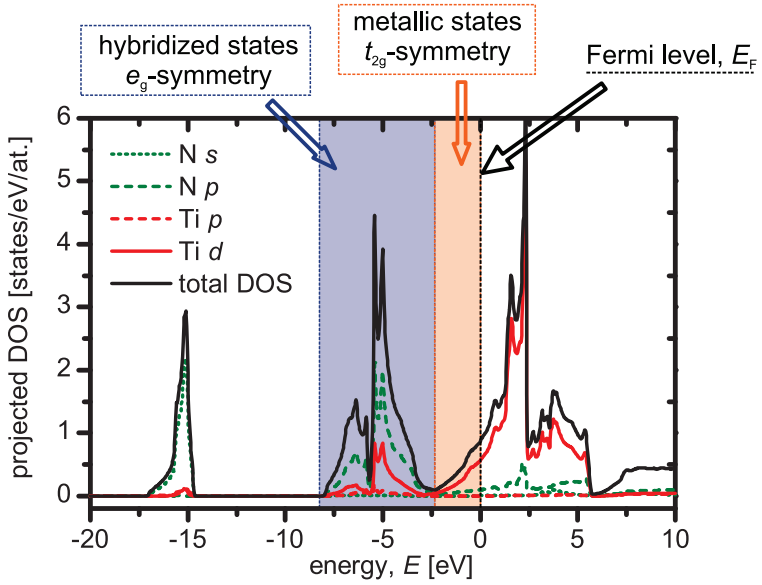

Figure 2.3: Projected density of states (DOS) for c-TiN. The electrons interacting in the hybridised region between ≈ -8 and ≈ -2 eV reflect the covalent character of the bonding. Higher states up to E_F mostly contribute to the metallic bonding of the binary TMN.

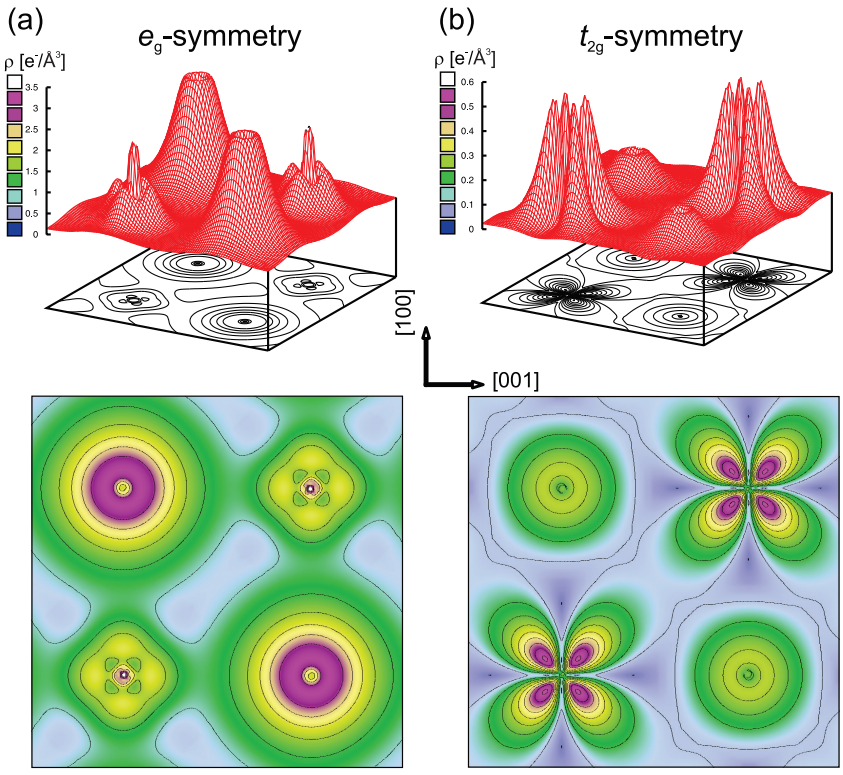

Figure 2.4: *Ab initio* obtained local charge distribution in c-TiN. Interaction of N p- and Ti d-electrons occurs either along (a) the $\langle 001 \rangle$ directions (e_g-symmetry) or (b) the $\langle 110 \rangle$ directions (t_{2g}-symmetry) in fcc-crystals of TMN. The overlap of the different bonding contributions is responsible for the covalent-metallic properties of TiN.

account for the metallic bonding character of TMN. The corresponding electrons of this energy level are predominantly localised along the ⟨110⟩ directions of cubic crystals and form the t_{2g}-symmetry (Fig. 2.4b). The states above E_F, if filled with electrons, are meant to contribute to anti-bonding of the interacting species.

A local charge enrichment or depletion within the metallic region, e.g. in (non)stoichiometric TMN or due to TM-alloying, can result in a collapse of the structure and the formation of different hybridisation schemes (compare section 3.3.2 and Publications IV, VII and VIII). The structural transformation from cubic to hexagonal goes along with a change from a sp^3d^2- towards the sp^3-hybridisation, as apparent in w-AlN, where only Al s- and N p-states remain to interact.

In the framework of this thesis, *ab initio* modelling was used on the one hand to predict various materials properties (Publications IV–VIII) and on the other hand to facilitate the interpretation of experimental findings (Publications III and IV).

2.3 Transition Metal Aluminium Nitrides

Since the physical and chemical properties of the individual TM mononitrides are strongly correlated to their (electronic) structure [22, 28], the need to overcome their single limitations arises with respect to specific requirements (e.g. oxidation resistance). As an example, in cutting and tooling industry high hardness in combination with high oxidation resistance are some basic requirements for a protective coating of the tooling insert. The temperatures at the interface tool/cutting-insert often exceed 900–1000 °C [11, 29], and are slowly dissipating in the vicinity of the contact area. Industrially widely utilised TiN coatings however suffer from oxidation already above ≈ 550 °C [30] by forming a porous rutile-type TiO_2 oxide scale.

Applying smart architectural coatings design [7], by e.g. the creation of separated TMN phases in two (multilayers) [31–34] or three dimensions (nanocomposites, precipitates) [35–37], is one way to improve the coating performance. Another approach is based on sophisticated alloying concepts and the formation of supersaturated solutions, or compositional gradients within single layer films [38–40]. Due to the extremely limited kinetics (cooling rates up to $10^{13}\,\mathrm{K}\cdot\mathrm{s}^{-1}$) apparent in PVD deposition techniques it is possible to synthesise a supersaturated solid solution of $Ti_{1-x}Al_xN$ [30, 41–45], although c-TiN and w-AlN exhibit no solubility in each other according to the quasibinary phase diagram in Fig. 2.5a [46]. The *ab initio* predicted energies of formation, E_f, for cubic and wurtzite solid solutions of the resulting metastable $Ti_{1-x}Al_xN$ films exhibit an energetically preferred cubic structure up to $x \approx 0.6$–0.7, see Fig. 2.5b. In the region where E_f exhibits almost similar values a dual phase regime of cubic and wurtzite structure is entered with higher Al content, followed by a

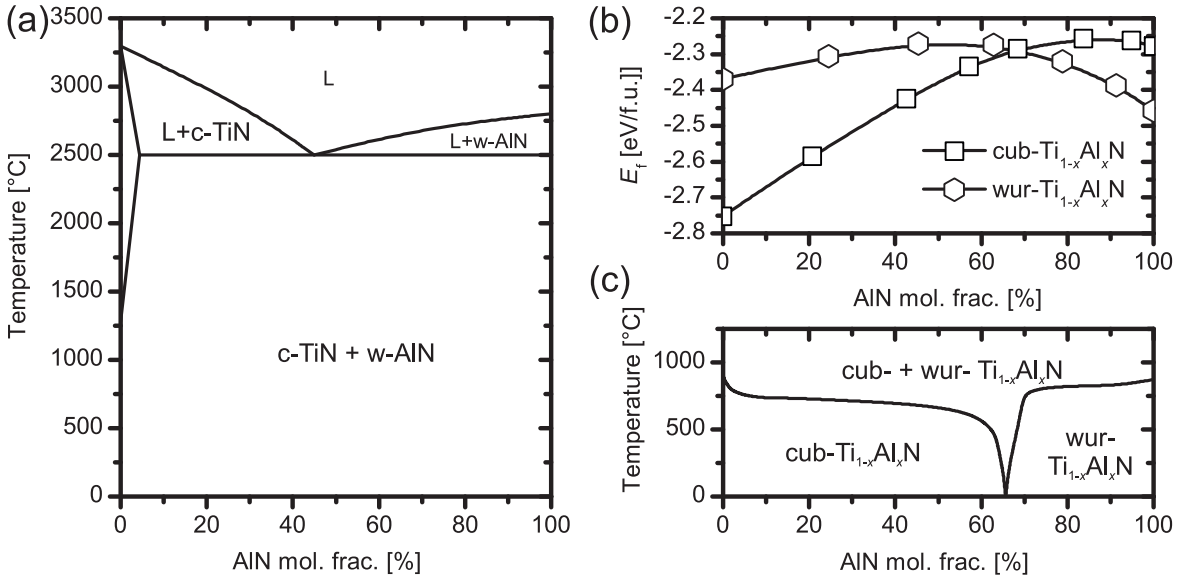

Figure 2.5: (a) Quasi-binary phase diagram along the tie line of TiN–AlN redrawn from Ref. [46]. (b) *Ab initio* obtained energies of formation, E_f, for the cubic and wurtzite solid solutions of $Ti_{1-x}Al_xN$ (adapted from Ref. [53]. (c) Metastable PVD-phase diagram from Spencer [52] based on experiments, confirming the *ab initio* predicted phase limits.

single phase wurtzite regime [47–51]. The corresponding metastable phase diagram, adapted from experimental observations by Spencer [52], is shown for $Ti_{1-x}Al_xN$ in Fig. 2.5c.

The incorporation of Al into other binary TMN is quite similar with respect to the development of certain element-specific (meta)solubility limits and superior properties of the ternaries compared to the binary nitrides, as valid also for TM = V, Cr, Zr, Nb, Hf, Ta, etc. [51, 54–63]. With increasing Al-content however also the driving force for decomposition increases drastically, which results in extraordinary properties at elevated temperatures, being the topic of the next chapter.

2.4 Phase Stability and Age Hardening of $Ti_{1-x}Al_xN$

The $Ti_{1-x}Al_xN$ system exhibits a wide miscibility gap at low temperatures, which in turn is responsible for its metastable character and outstanding performance at high temperatures [64]. A simplified picture to understand the supersaturated solid solution of cubic NaCl-structured $Ti_{1-x}Al_xN$ (for $x \lessapprox 0.66$) assumes two sublattices, which are either fully populated by nitrogen while the other sublattice is randomly occupied by composition dependent Al and Ti atoms [53]. This assumption enables for the calculation of E_f and H_{mix} of the ternary compound, which correspond to the phase stability of predefined structures. Also the driving

force for decomposition into the (meta)stable compounds can be expressed as function of Al content, x, and temperature (see Fig. 2.6) [46, 65, 66].

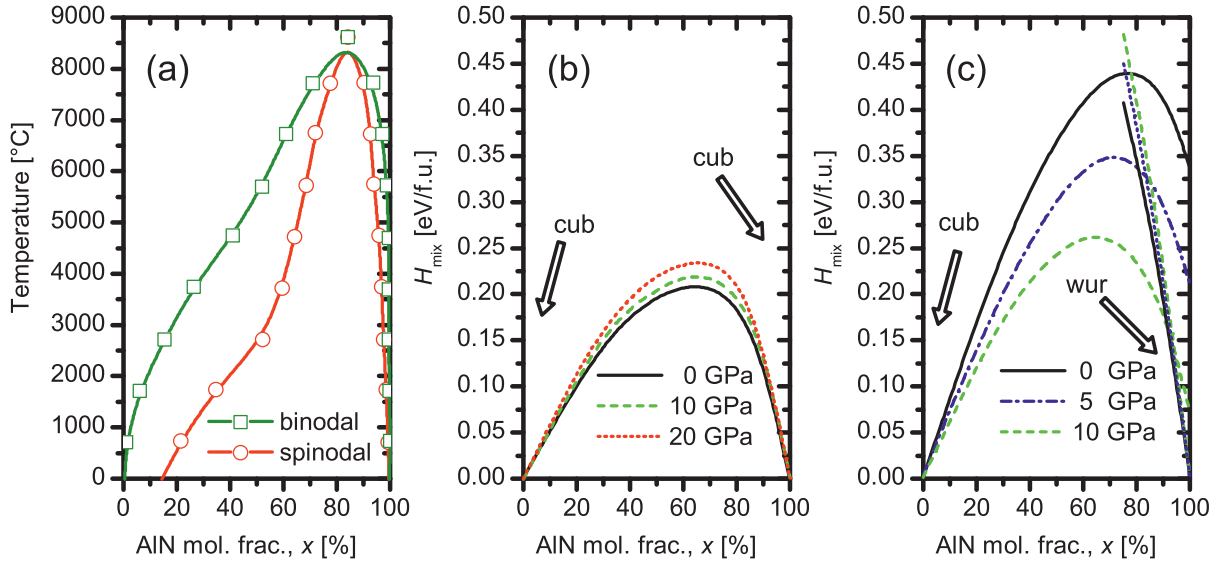

Figure 2.6: (a) Composition-temperature phase diagram of c-$Ti_{1-x}Al_xN$ (from Ref. [65]). Mixing enthalpies of $Ti_{1-x}Al_xN$ as a function of Al content, x, at different pressures (adapted from Ref. [66]. (b) H_{mix} for the isostructural decomposition into c-TiN and c-AlN. (c) Influence of pressure on H_{mix} with respect to c-TiN and w-AlN.

Two different regions, called binodal and spinodal, can be identified in the composition-temperature phase diagram according to Refs. [53, 65, 67], see Fig. 2.6a. In the region where the second derivative of the Gibbs free energy is positive ($\partial^2 G/\partial c^2 > 0$) the decomposition of $Ti_{1-x}Al_xN$ takes place by nucleation and growth (e.g. $Ti_{1-x}Al_xN \rightarrow$ c-TiN + w-AlN), requiring an activation energy for the formation of w-AlN precipitates. However, within a second region marked by the spinodal line, where $\partial^2 G/\partial c^2 < 0$, already small composition fluctuations result in isostructural decomposition towards c-TiN and c-AlN if kinetics allow it [64, 68, 69]. This implies that within the spinodal region essentially no energy barrier for decomposition exists, apart from thermal activation enabling for diffusion. The thermally induced spinodal decomposition of such alloys gained great importance in industry, as it results in an increased hardness. This effect is often referred as *age hardening*, due to the interaction of time and temperature.

The positive H_{mix} over the whole composition range indicates a high driving force for decomposition of c-$Ti_{1-x}Al_xN$ into the cubic boundary phases c-TiN and metastable c-AlN (Fig. 2.6b). With increasing pressure, this driving force significantly increases, while H_{mix} for the decomposition of c-$Ti_{1-x}Al_xN$ into c-TiN and w-AlN is effectively reduced, compare Fig. 2.6b and c.

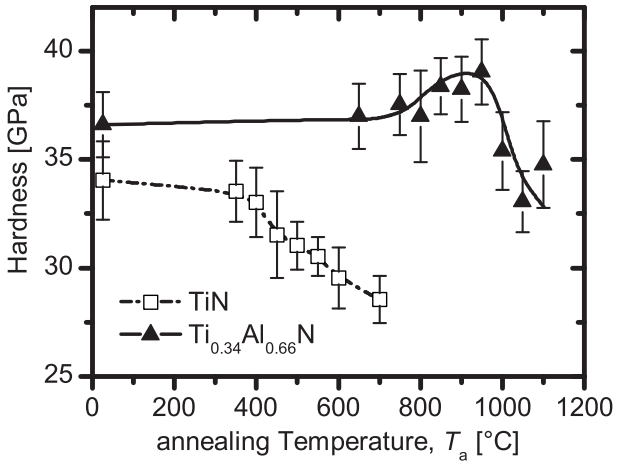

Figure 2.7: Film hardness over annealing temperature for c-TiN and c-$Ti_{0.34}Al_{0.66}N$ (adapted from Ref. [71]). The hardness increase with temperature is referred to as *age hardening*.

Materials exhibiting a large single-phase field, such as TiN, suffer from softening in course of thermal load due to recovery, recrystallisation and grain growth processes. In contrast, metastable c-$Ti_{1-x}Al_xN$ shows a substantial hardness increase with increasing temperature, called age hardening, as shown in Fig. 2.7. It was observed that within the single phase cubic regime, up to temperatures of $\approx 900\,°C$, TiN- and AlN-enriched domains form, whose locally different lattice parameters cause strain hardening of $Ti_{1-x}Al_xN$ due to hindering of dislocation motion [7, 69, 70]. If the chemical composition of stoichiometric AlN is reached locally, the metastable c-AlN domains are meant to transform into the stable w-AlN phase. Coarsening of the structure, the loss of coherency strains between c-TiN and w-AlN, which further exhibits inferior mechanical properties compared to c-AlN, causes steadily decreasing hardness within the dual phase regime [71].

In the past, theoretical [53, 64, 66, 67, 72] and experimental [71, 73] investigations where dealing with the effect of e.g. composition, temperature, vacancies, isostatic pressure, internal strain and surface energies on the extent of the driving force for spinodal decomposition. In general, the driving force (H_{mix}) for decomposition into c-TiN and metastable c-AlN increases with increasing Al content up to the metasolubility limit of the cubic phase field (compare Section 2.3). Also increasing compressive stresses (corresponding to isostatic pressures in Refs. [66, 74]) in the coating are supposed to promote the isostructural decomposition, while on the other hand they act as a retarding factor for the precipitation of w-AlN with $\approx 24\%$ bigger specific volume than c-AlN [64, 74, 75]. Since another contribution to the decomposition driving force is related to the reduction of total surface energy and the creation of new interfaces during phase separation, the overall driving force for decomposition is difficult to determine [10, 64] and needs sophisticated experimental proof. A comprehensive overview

on the structural evolution of $Ti_{0.46}Al_{0.54}N$ thin films as a function of temperature and time exploits these issues in detail, see Publications I to III.

2.5 Multinary Transition Metal Aluminium Nitrides – The Holy Grail?

As discussed above, smart alloying concepts enable for the creation of enhanced material properties. For this reason, a lot of research activity was done in the past decades to overcome certain deficiencies of $Ti_{1-x}Al_xN$. In combination with coating architecture, especially the alloying of $Ti_{1-x}Al_xN$ with additional elements was regarded as a promising approach to improve e.g. friction, wear, oxidation resistance, and hardness of $Ti_{1-x}Al_xN$.

Non-metal alloying of C, Si and B takes mainly place by incorporation of the non-metals on the N sublattice. The resulting grain refinement and the formation of various nanostructures achieve increasing hardness and in general improved oxidation resistance. Other practical aspects like low friction and wear still require improvement [76–83].

On the opposite, group III–VI TM-alloying is mainly achieved by substitution of Ti or Al at the metallic sublattice, which allows for a huge variety in size and different bonding types, due to their different electronic configuration (e.g. valence electron number, additional *d*- and *f*-states). Investigations of Y and Cr have already shown the big potential of TM-additions to effectively enhance the oxidation resistance [84–87] of $Ti_{1-x}Al_xN$. In terms of reduced friction especially at elevated temperatures, the addition of V [34, 88–92] proved to be useful due to the formation of a V_2O_5-Magnéli oxide phase at high temperatures. Other TM-elements, such as e.g. W or Mo, yield akin results with respect to the development of Magnéli phases, which however suffer from volatility at temperatures above 500 and 700 °C, respectively [93]. Moreover, stoichiometric MoN and WN preferably crystallise in the hexagonal structure and are hence difficult to implement in cubic $Ti_{1-x-y}Al_xTM_yN$ [94].

Alloying with group VI and V elements such as Zr, Nb, Hf, and Ta is acknowledged for the enhancement of mechanical properties and wear resistance [95–103], although the impact of the various alloying elements on structure and mechanical properties is not yet fully understood. Moreover, the combination of experiments with theoretical work with respect to thermal stability is a totally unexplored field. Hence, the goal of this thesis is to yield a comprehensive understanding for the electronic origin of thermal stability in $Ti_{1-x-y}Al_xTM_yN$ and exploring methods to enable for a theory guided materials design instead of the traditional trial-and-error approach.

Chapter 3

Methodical Approach

3.1 General considerations

The simultaneous investigation of nanostructure and chemistry and its effect on various material properties is an extreme challenge in materials science. While most studies on structure-property relationships of thin films use single crystal (sc) substrates, a totally different situation arises for investigations of structural phenomena on polycrystalline (pc) substrates. Especially, studies employing high-temperature annealing treatments, as performed in this thesis for *age hardening* of $Ti_{1-x}Al_xN$, require a sophisticated investigation concept.

In order to determine the mechanical properties and structural response of $Ti_{1-x-y}Al_xTM_yN$ coatings on annealing temperature (Ta) and annealing time (ta), care has to be taken in choosing suitable substrate materials and investigation techniques. On the one hand, single crystal substrates such as silicon (100, 111) or MgO (100, 111) or equivalent sublayers of e.g. TiN can predetermine the initial growth conditions for thin films, resulting in predominant orientations or even epitaxial growth of the developing film. This may strongly affect the thin film properties and stands in general contrast with common deposition techniques for polycrystalline tool materials, where at most local epitaxy [104] is observed on different microstructural features, but in general no epitaxial film growth occurs.

On the other hand, thermally induced substrate interaction, such as substrate material indiffusion [73, 83] or spinel formation [105, 106] at the substrate interface, should be avoided, in order to asses solely the properties of the coating. This limitation can be overcome by chemically removing the substrate after deposition to obtain free-standing thin film material.

Hence, two different polycrystalline substrates, namely low alloy steel foil (thickness 0.2 mm)

and polycrystalline Al_2O_3 platelets ($20 \times 7 \times 0.5\,mm^3$) were selected for investigations of the thermal stability of $Ti_{1-x-y}Al_xTM_yN$, resembling more to the growth conditions on tools than on single crystals. Post-deposition dissolution of the Fe foils in 10 mol.% nitric acid results in free-standing coating material that can be used for the structural investigations of the pure coating material by atom probe tomography (APT) and transmission electron microscopy (TEM), or after crushing to powder for X-ray diffraction (XRD) analysis. The thermally stable alumina substrates were used for measuring the electrical resistivity by the four-point probe technique and mechanical properties by nanonindentation subsequent to the annealing treatments. Further single crystalline Si ($20 \times 7 \times 0.5\,mm^3$) and Al_2O_3 ($10 \times 10 \times 0.5\,mm^3$) platelets were chosen for the investigation of mechanical properties (e.g. biaxial stress measurements, XRD or TEM) at room temperature.

In order to conduct detailed studies on the combined influence of structure and chemistry on mechanical properties, experimental investigations which enable for a three-dimensional understanding are required. Although high-resolution TEM (HR-TEM) is a powerful tool for analysis of nanostructures and especially orientation relationships, sample thicknesses of $< 50\,nm$ (to reach electron transparency) still contain too many overlapping grains in analysis direction to enable accurate distinction between the individual features. Also chemical analysis of 3D-structures in TEM by e.g. energy dispersive X-ray spectroscopy (EDX) or electron energy loss spectroscopy (EELS) is limited for similar reasons. The restricted lateral resolution of secondary ion mass spectroscopy (SIMS) hinders its applicability for the present work. The observation of chemical fluctuations at the atomic scale is however a crucial feature to understand atomistic processes determining various physical phenomena, such as age hardening, in materials science.

3.2 Atom Probe Tomography and Complementary Techniques

Based on the principle of field ion microscopy (FIM), invented by Müller already in 1951 [107], the direct image formation of specimen surface ions is combined with a time-of-flight mass spectrometer in modern atom probe tomography (APT) [108, 109]. Highest chemical sensitivity is thus combined with near-atomic resolution in three dimensions [110, 111], which seems highly suited for the investigation of spinodal decomposition, as shown for the Fe-Cr system in Refs. [112–114].

A FIM operates as a lens-less point projection microscope by ionisation of image gas atoms (He or Ne) at the surface of a needle shaped specimen. Due to a high standing voltage (V), sharp needle-shaped specimens with a tip radius (r_{tip}) of less than 100 nm are required

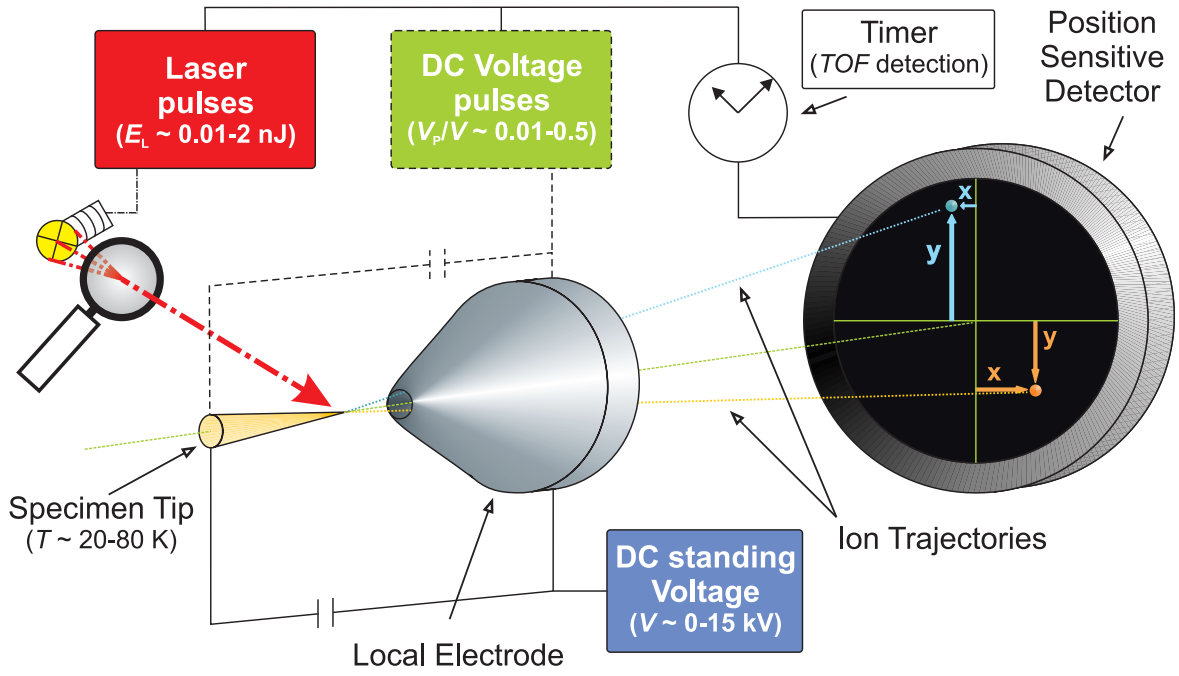

Figure 3.1: Schematic drawing of the working principle of a state-of-the-art local electrode atom probe (IMAGO LEAP 3000X-HR), as used in this thesis (adapted from Ref. [116]). On top of a standing voltage (below F_0) either voltage pulses V_P or laser pulses with a certain laser energy E_L are triggered by a time-of-flight unit to control the field evaporation process at the specimen.

to achieve a sufficiently high electric field for ionisation (F_0) of the gas atoms at the apex, according to the formula [115]:

$$F_0 = \frac{V}{k \cdot r_{\text{tip}}} \tag{3.1}$$

where k is a geometrical constant.

In contrast to FIM, the working principle of APT, as schematically shown in Fig. 3.1, uses directly evaporated specimen ions, which are subsequently accelerated towards a position sensitive detector (PSD). In order to brake the surface-atom bonds and achieve ionization, high electric fields of e.g. $F_0^{\text{Ti}} = 26\,\text{V} \cdot \text{nm}^{-1}$, $F_0^{\text{Al}} = 19\,\text{V} \cdot \text{nm}^{-1}$ or $F_0^{\text{W}} = 52\,\text{V} \cdot \text{nm}^{-1}$, are required [110]. The evaporation process essentially can consist of a two stage mechanism: First the thermally activated or electric field induced ions escape over an activation-energy barrier (see Fig. 3.2a), and then often post-field ionization processes into higher charge states can take place [115–117].

Since a sufficiently high electric field would result in continuous but uncontrolled evaporation (see Fig. 3.2b), two approaches were developed with the goal to time-resolve the evaporated species. Initially the standing voltage is kept slightly below F_0. Secondly a pulsing unit,

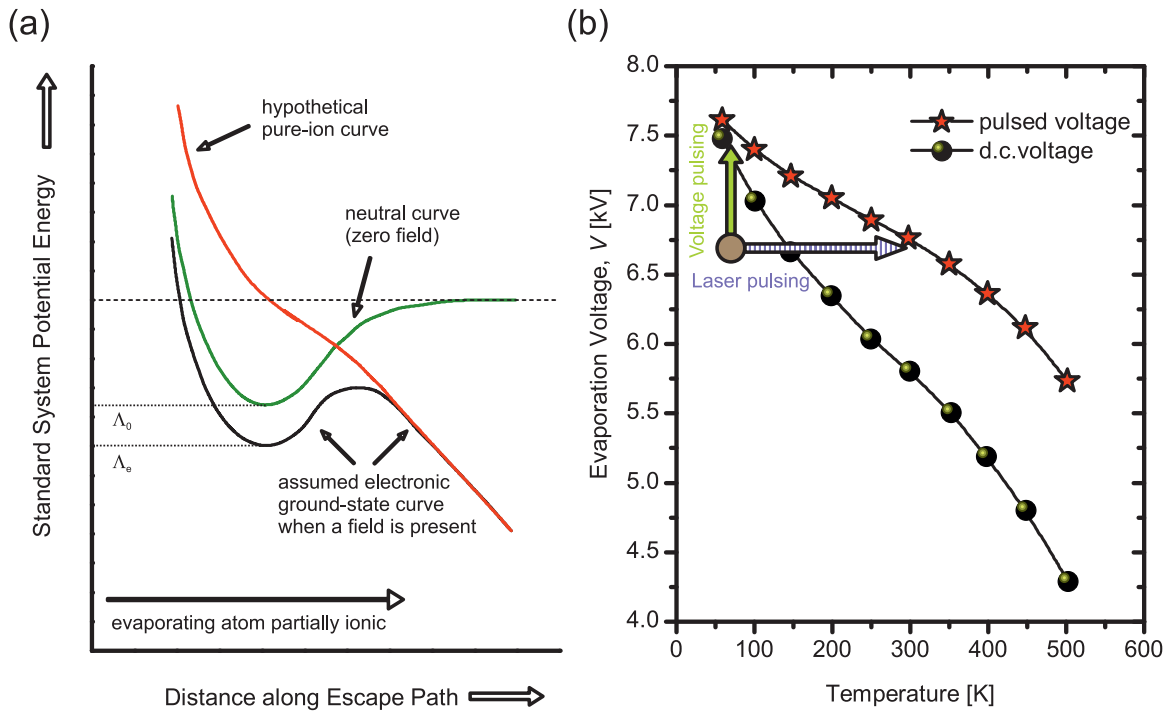

Figure 3.2: (a) The field evaporation mechanism of surface atoms as adapted from Ref. [116]. The energy zero corresponds to a neutral atom (being bonded by Λ_0) in remote field-free space. Applying an external electric bias potential lowers the energy barrier for the atom (Λ_e) to become integrally charged with increasing distance from its original location. (b) Required voltage for field evaporation of W as a function of temperature, for a given evaporation rate of 100 at./sec. (d.c. voltage – ball symbols) or 10^9 at./sec. (superimposed voltage pulses – star symbols). The data are obtained from Ref. [118]. In case of electrically non-conductive specimen (circle) at low temperatures, the necessary evaporation voltage often exceeds the mechanical strength of the material (green arrow). The application of laser pulses increases the temperature only and thus drastically reduces the required evaporation voltage (violet dashed arrow) [119].

operating in the kHz range, can be used to apply a certain voltage fraction ($V_p/V = 0.01$–0.5) on top of the standing voltage to control the ionization process (compare Figs. 3.1 and 3.2b). This method is however limited to electrically conductive materials, as the tensile load on the specimen due to the electric field often exceeds the mechanical strength of brittle materials e.g. TMN [116, 117, 120–122]. Another possibility to overcome the energetic barrier is by thermal activation using laser pulses in the pico- to femtosecond range [123, 124] (see Fig. 3.1). The necessary nominal voltage for evaporation can thus effectively be reduced due to the laser energy (see arrows in Fig. 3.2b) [123, 125, 126] and enables for the investigation of low-conductivity materials, such as oxides and nitrides [118, 127, 128].

To prevent from surface migration and diffusion of specimen material, which would corrupt

the quality of the measurement, the whole assembly has to be cooled to cryogenic temperatures (20–80 K) [119, 128]. By means of either voltage- or laser-pulsed APT it is possible to measure the time of flight (TOF) of the evaporated specimen ions, which in combination with the atomic coordinates (x, y – see Fig. 3.1) from the position sensitive detector (PSD) results in almost atom-by-atom chemical sensitivity in three dimensions [128]. Computer-aided reconstruction of the acquired data, e.g. by the software package IVAS^{TM}[129], further allows for direct and statistical data processing, which is further explained in the discussion on APT measurements of $Ti_{1-x}Al_xN$.

3.2.1 APT of $Ti_{1-x}Al_xN$

Classical preparation techniques for metallic specimens use a two-step chemical etching technique as given in [108], to obtain needle-shaped specimens that fulfil all geometric preconditions for APT measurements. Because of the high chemical stability and geometric limitations due to the limited thickness of thin films on a substrate, this preparation technique is improper in case of micrometer thin $Ti_{1-x}Al_xN$ coatings. As suggested in literature [130–132] more sophisticated techniques, using focused ion beam microscopy (FIB), can be utilised for site-specific specimen preparation of e.g. grain boundaries and metallic thin films. In case of metallic multilayer films for storage applications, the interesting features are planar and thus lie perpendicular to the measurement direction of APT [130, 132–134]. The specimen preparation by deposition of thin films on presharpened Si microtips [133, 135], prior to Ga-beam sharpening in the FIB, appears as a time-saving alternative to the lift-out techniques generally used.

In case of TMN however difficulties arise from direct deposition of e.g. TiN films on preshaped Si microposts, as visible in the TEM cross-sections in Fig. 3.3 [136]. Although the growth behaviour of the films on Si substrate and Si microposts are comparable with respect to column width and orientation, the TiN film on the Si micropost exhibits extensive cracks within the Si micropost but also between the TiN columns (indicated by arrows). The good adherence between TiN film and Si micropost causes cracking below the interface. This is because of the thermal mismatch of the Si substrate and the TiN coating during cooling from deposition temperature ($T_{dep} = 500\,°C$) to room temperature, which usually results in compressive stresses of the substrate (visible as strain contrast lines in Fig. 3.3a).

Because of the columnar growth of the films during deposition, similar to the TiN films above, common FIB-based techniques were not suitable for the present work. By virtue of the present works focus on the three-dimensional nature of spinodal decomposition in $Ti_{1-x}Al_xN$ thin films, a FIB-based preparation technique was modified to fulfil our requirements, as explained in detail in Publication I. Usually the film growth direction (GD) is in line with the

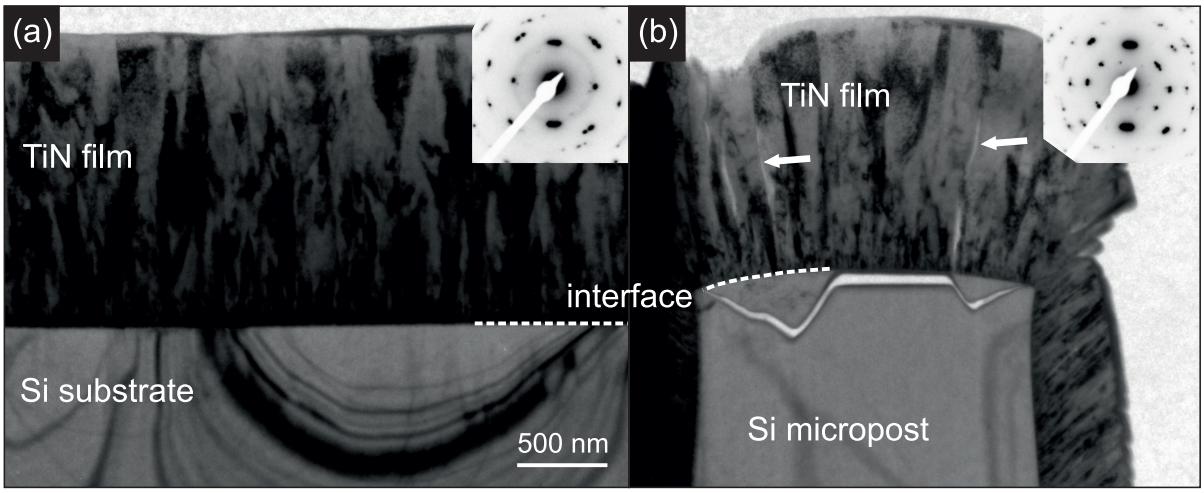

Figure 3.3: TEM cross-sections of TiN films after deposition on (a) a planar Si (001) substrate and (b) a Si micropost as usually used for sample carrier for APT. Although the structural features are equal for both substrates, the intercolumnar and interfacial cracks to the Si micropost make APT impossible [136].

APT measurement direction (MD), thus the chemical fluctuations at the column boundaries are difficult to access. Another point is that the $Ti_{1-x}Al_xN$ films were annealed at high temperatures, which would result in extensive substrate material indiffusion as explained in Refs. [73, 136, 137]. Thus the APT-specimen preparation was performed from free-standing $Ti_{1-x}Al_xN$ coating material, in the as deposited state and additionally after annealing to 900 and 1350 °C. The crucial issue is to mount the $Ti_{1-x}Al_xN$ coating material with the GD perpendicular to the MD, which enables to cross column interfaces during the measurement.

Since laser-assisted APT is strongly affected by specimen geometry, laser energy and material properties [138], the suitability of steel and Si was studied as support materials for APT of TMN. Moreover, the relatively low thermal and in case of $Ti_{1-x}Al_xN$ also electrical conductivity, causes significant troubles during APT. Thermal "tails" appear in the mass spectrum, which can significantly reduce the signal-to-noise ratio and corrupt the resolution of the analysis [138]. The influence of measurement temperature, evaporation rate, pulse frequency and laser energy was explored for this reason in order to achieve optimum conditions for data acquisition. It turned out that a laser energy of 0.7 nJ, a pulsing frequency of 200 kHz, a temperature of 60 K and the utilization of predefined Si microposts as support materials reached most suitable results (Publications I, II, III).

Using APT for the investigation of nanostructures formed during annealing provides essential information for the understanding of spinodal decomposition and its impact on the mechanical properties of $Ti_{1-x}Al_xN$. For the presentation of the APT data, 1D-, 2D-, and 3D-concentration profiles [115, 139] were used in combination with statistics [115, 140, 141]

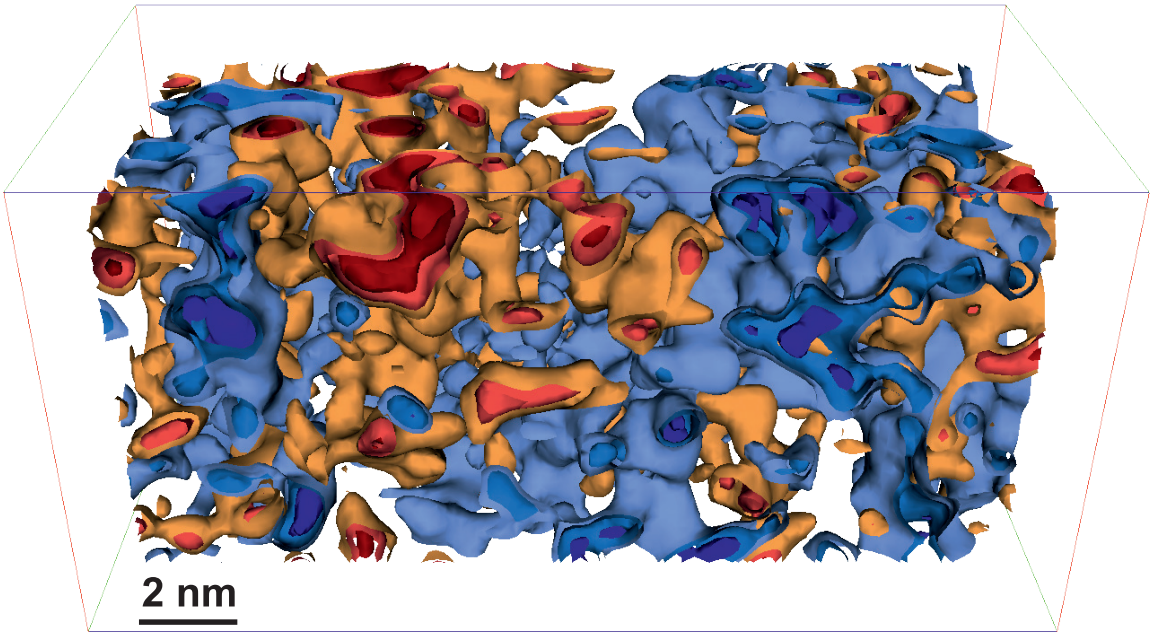

Figure 3.4: A 3D-interconnected structure of TiN- and AlN-rich domains has formed in $Ti_{0.46}Al_{0.54}N$ after annealing to 900 °C. Isoconcentration surfaces were drawn at (red) Al- and (blue) Ti-concentrations of 2, 5, and 7 at.% above the average film composition. Empty regions between the TiN- and AlN-enriched domains correspond to the remaining $Ti_{0.46}Al_{0.54}N$ matrix with lower element concentration as the chosen threshold values.

on the extent of decomposition in the various annealing states. This approach delivers information on the location of e.g. oxygen impurities (Publication I) or the magnitude of elemental fluctuations on the metallic sublattice of $Ti_{1-x}Al_xN$ already after deposition (Publication II and III), highlighting the excellent applicability of APT for the investigations of TMN thin films.

For graphical presentation of the 3D-nature of the TiN- and AlN-enriched domains, formed in course of the annealing treatments, isosurface plots [115, 142] were used, which connect subsamples (voxels) of the measured sample volume exhibiting equal concentration of a certain element, see for example Fig. 3.4. For further information and discussion see Publications II and III.

The structural and chemical investigations of annealed c-$Ti_{1-x}Al_xN$ by XRD, HR-TEM, and APT provided insights in the evolution of microstructure as a function of annealing temperature and time. The spinodally formed structural features were further correlated with the evolution of mechanical and electrical properties. A UMIS nanoindentation device [144] was used to determine film hardness and indentation modulus (see Fig. 3.5a) for $Ti_{1-x}Al_xN$ films on pc-Al_2O_3 and correlated to the microstructural strain, ε, (Fig. 3.5b), determined

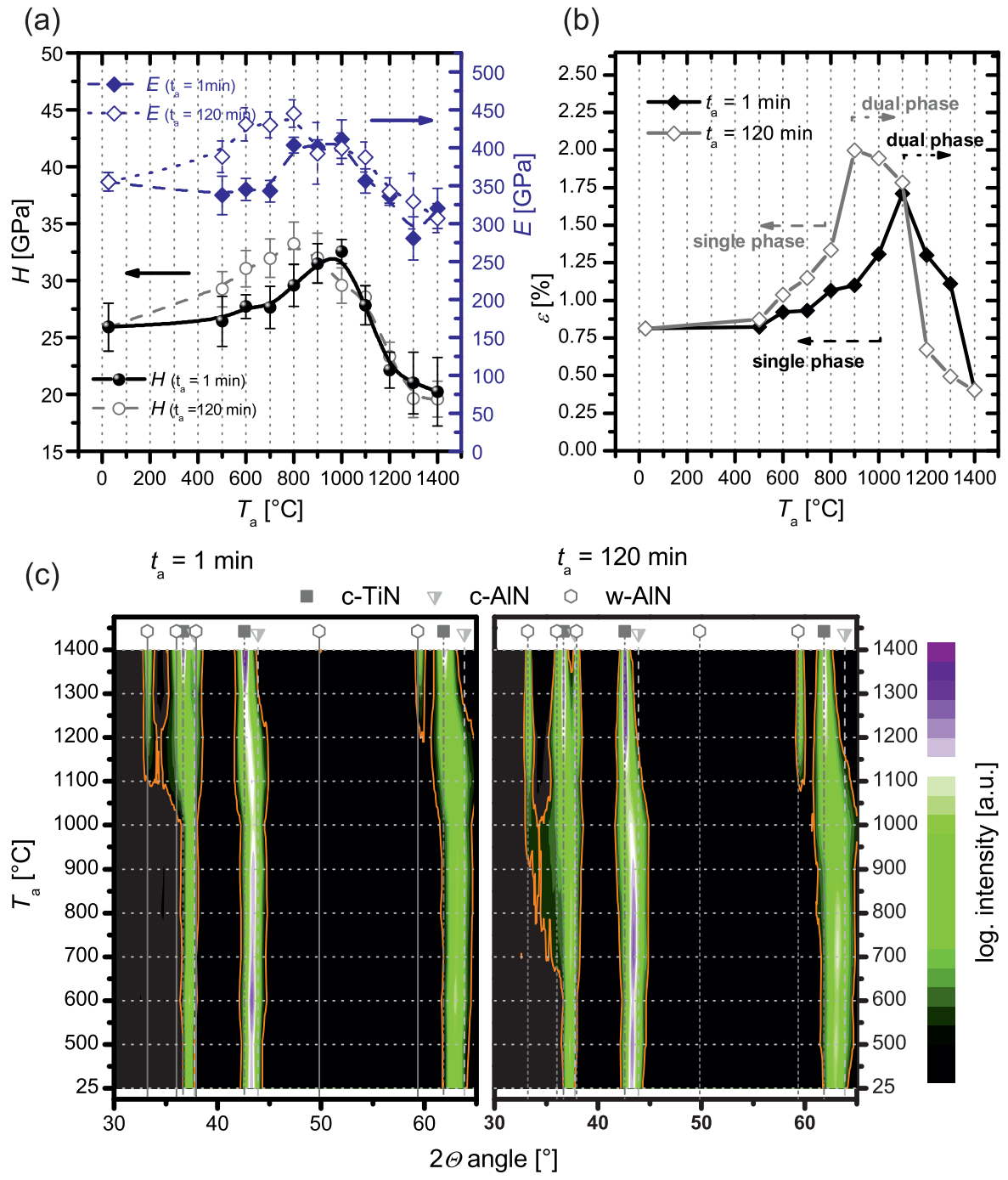

Figure 3.5: (a) Film hardness of $Ti_{0.46}Al_{0.54}N$ as a function annealing temperature, T_a, and time, t_a. (b) Corresponding microstrain determined by the Williamson-Hall method [143]. (c) Structural evolution of the films plotted as quasi-2D XRD plot. The intensities are reflected by the corresponding colours. The detectable formation of w-AlN at 1100 °C ($t_a = 1$ min) and 900 °C ($t_a = 120$ min) corresponds to the hardness decrease in (a) and the highest strains in (b).

by the Williamson-Hall procedure [143] from X-ray diffraction of powdered $Ti_{1-x}Al_xN$ films (Fig. 3.5c), after annealing for either 1 or 120 min at T_a.

By means of cross-combining experimental and theoretical work, it was shown that the 3D-nature of the isostructurally formed c-TiN- and c-AlN-domains (compare Fig. 3.4) results in increasing coherency strain between the microstructural features. In advance to other results on small angle X-ray scattering (SAXS) [75, 145], EELS [146], or XRD [71, 147], it was possible to identify the importance of coherent interfaces and the impact on the thermal stability during the first stages of decomposition, before loss of coherency and the precipitation of w-AlN results in reduced mechanical properties and decreasing strain (see Fig. 3.5). This approach enabled to draw a comprehensive picture on the impact of temperature and time on the decomposition pathway of $Ti_{1-x}Al_xN$. Further information and experimental details are included in Publication III.

3.3 Modelling $Ti_{1-x-y}Al_xTM_yN$ Alloys and Comparison to Experiment

3.3.1 Applied Modelling Methodology for $Ti_{1-x-y}Al_xTM_yN$ Alloys

The use of density functional theory (DFT) modelling in materials science is nowadays widely accepted for investigations of the electronic structure of condensed matter. Using software packages as the Vienna Ab Initio Simulation Package (VASP) [148, 149] or the Wien2k code [150], allow for the calculation of alloy specific features e.g. formation energies (E_f), mixing enthalpies (H_{mix}) or the charge transfer between atoms on the lattice [9].

In this thesis DFT modelling was used together with the projector augmented wave pseudopotentials [151], employing the generalized gradient approximation (GGA) as parametrized by Perdew and Wang [152]. Mainly two modifications, namely cubic (fcc, B1-structure, $Fm\overline{3}m$ space group, NaCl-prototype) and hexagonal (wurtzite, B4-structure, $P6_3mc$ space group, ZnS-prototype) were considered for the $Ti_{1-x-y}Al_xTM_yN$ alloys, and mimicked by special quasi-random structures (SQS) [153, 154]. The respective supercells were set up by 36 atoms ($3 \times 3 \times 2$) for the cubic and 32 atoms ($2 \times 2 \times 2$) for the hexagonal structures. Since only one or two atoms at the metallic sublattice (i.e. 18 or 16 sites, respectively, as the other sublattice is fully occupied by N) were exchanged by TM-atoms, compositional steps of 5.56 or 6.25 at.% can be achieved for x and y in the $Ti_{1-x-y}Al_xTM_yN$ alloys. Further details on the calculations can be found in Refs. [103, 155] and Publications IV to VIII.

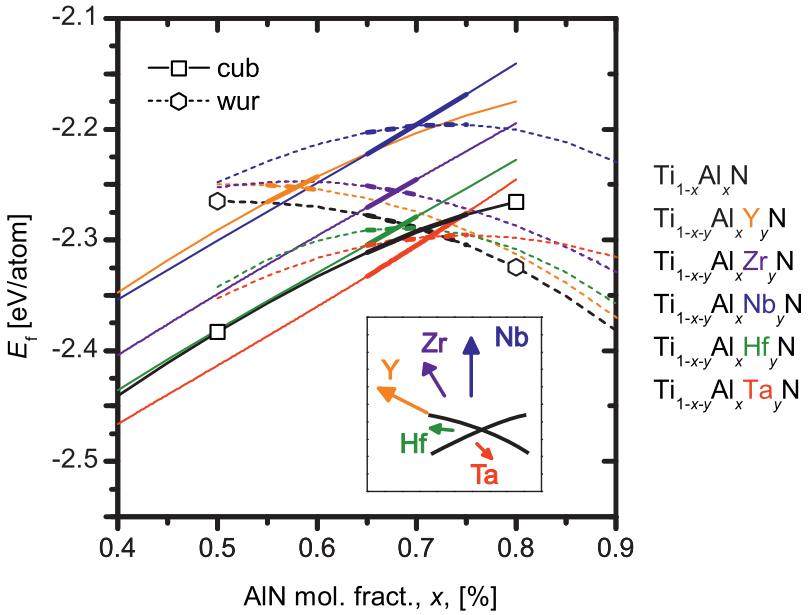

Figure 3.6: Formation energies, E_f, for $Ti_{1-x-y}Al_xTM_yN$ with $y = 0$ and 0.111 (cub), or $y = 0$ and 0.125 (wur) as a function of Al content, x. For a given composition the more stable structure is determined by the lower E_f. The insert qualitatively indicates the shift of the cubic (meta)solubility limit and the total energy of the system. Data were included from Refs. [103, 156, 157] and Publications IV to VIII for various TM-elements, respectively.

3.3.2 Impact of TM-alloying on the Phase Stability of $Ti_{1-x-y}Al_xTM_yN$

The structural transition from cubic to wurtzite in $Ti_{1-x-y}Al_xTM_yN$ can be predicted by calculation of E_f as a function of the Al content, as presented in Fig. 3.6 for TM = Y, Zr, Nb, Hf and Ta, respectively. The structure with lowest E_f values is most likely to be formed during deposition. For clarity, only the data for the ternary $Ti_{1-x}Al_xN$ and the quaternaries with $y = 11.1$ at.% (cubic) and $y = 12.5$ at.% (wurtzite) at the metallic sublattice are shown. In the presented graph, a clear trend can be found for the impact of TM on the cubic solubility limit.

The formerly discussed cross-over of the cubic and wurtzite structure is significantly lowered from $x \approx 0.69$ [53] for $Ti_{1-x}Al_xN$ to $x \approx 0.56$ for the addition of 12.5 at.% Y to the metal sublattice ([156] and Publication IV). Additions of 12.5 at.% Hf ($x \approx 0.69$) [Publication VIII], Nb (to $x \approx 0.68$) [Publication V], or Zr ($x \approx 0.68$) [103] to the metal sublattice have only negligible influence on the extent of the cubic solubility range of $Ti_{1-x-y}Al_xTM_yN$ alloys. The only slight increased cubic stability range to $x \approx 0.70$ [Publication VII] of $Ti_{1-x}Al_xN$ can be observed by the addition of Ta for the here studied TMN.

The magnitude of E_f is influenced similarly, as highlighted by the arrows in the insert of

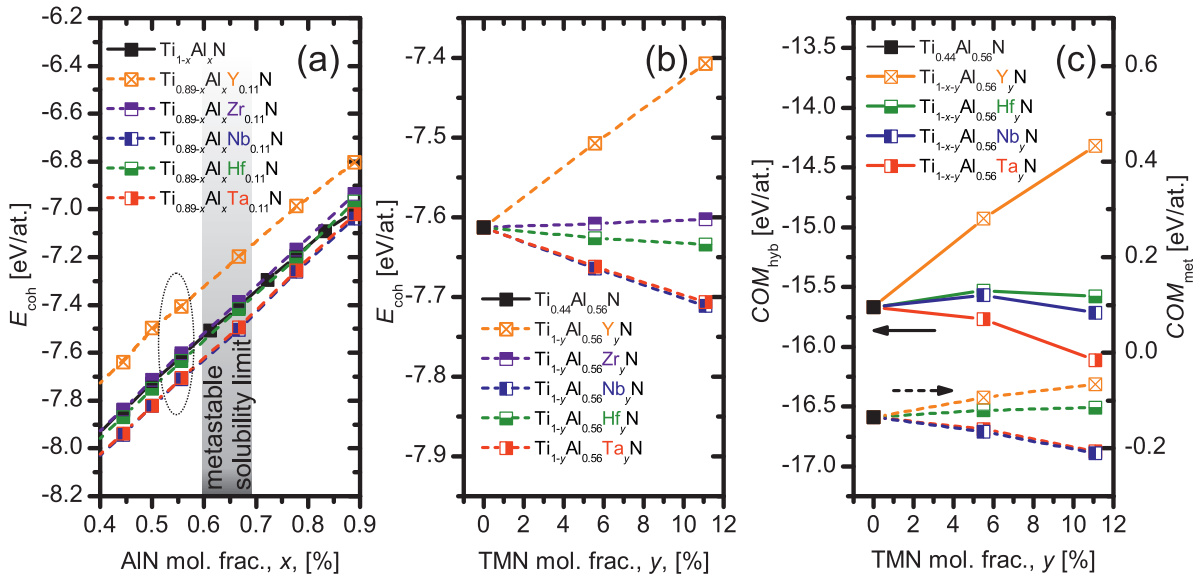

Figure 3.7: (a) Cohesive energies, E_{coh}, for c-$Ti_{1-x-y}Al_xTM_yN$ as a function of Al content, x, for $y = 0$ and 0.11. (b) The effect of various TM on E_{coh} in the region close to the cubic (meta)solubility limit as function of y. (c) The weighted sum of DOS of the hybridised (COM_{hyb}) and metallic (COM_{met}) region (compare Fig. 2.3) indicate a measure for stability of the alloy. Detailed information is included in Publications IV-VIII.

Fig. 3.6. The addition of group IIIB, IVB and VB TM-elements also strongly affects E_{coh} of the quaternary cubic solid solutions, as shown in Fig. 3.7a for TM additions of $y = 0$ and 11.1 at.% at the metal sublattice, respectively. While Y (three valence electrons, VE) reduces the cohesive forces, by significantly changing the electronic structure (see Publication III), Hf and Zr (four VE, and isovalent with Ti) have almost no impact on the extent of E_{coh}. In contrast, the group VB elements Nb and Ta (five VE) increase E_{coh} over the whole Al composition range. As the driving force for decomposition strongly increases up to the cubic metastable solubility limit, an Al content of $x = 0.56$ was chosen to emphasise the effect of Ti substitution by TM-alloying, see Fig. 3.7b. The above given trend for the different effect of the VE configuration on the E_{coh} strongly scales with the amount of TM at the metallic sublattice.

Sorting the different TM-elements with respect to their extent on E_{coh}, a clear trend can be deduced. While Y weakens the bonding, Zr and Hf exhibit almost no effect on the electronic configuration. Only Nb and Ta significantly strengthen the bonding in cubic $Ti_{1-x-y}Al_xTM_yN$ alloys. The diverse alloying effects can be correlated with changes in the electronic structure, as summarised by the weighted average of the hybridised and metallic regions of the DOS (compare section 2.2). The centre of mass of the hybridised states (COM_{hyb}) gives rise on the covalent part of the bonding, which shifts to a higher energy by

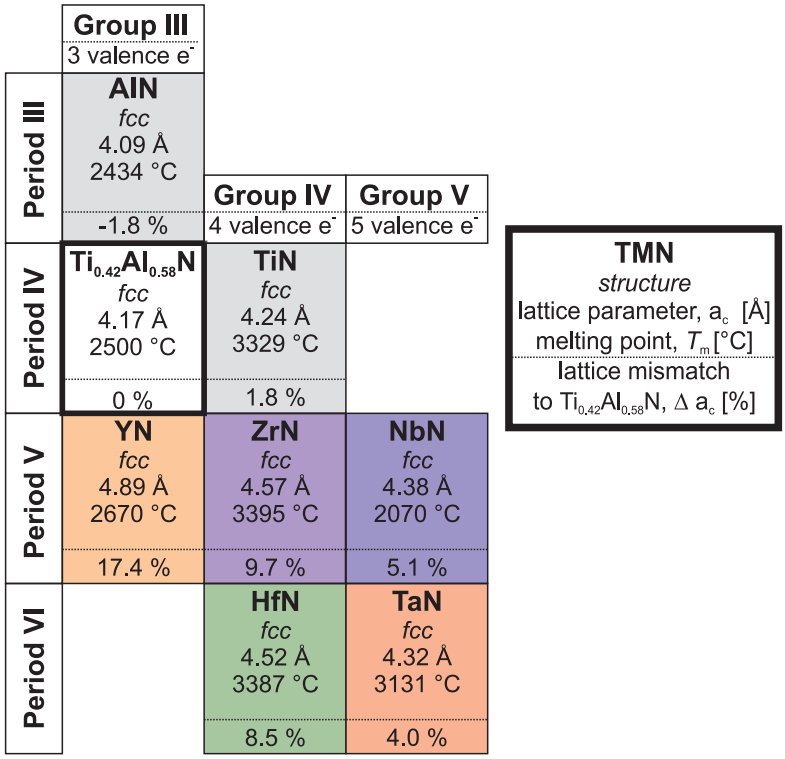

Figure 3.8: Schematic summary of cubic binary TMN, including some important properties and their lattice mismatch with respect to $Ti_{0.42}Al_{0.58}N$. Data obtained from [27, 158–160] as well as Publications IV-VIII.

Y-alloying but to lower energies by introduction of Hf, Nb and Ta. This behaviour stems from the available TM *d*- and in case of Hf and Ta also *f*-states. An even more pronounced effect appears for the near-metallic region, where COM_{met} refers to the states close to the Fermi level, E_F, see Fig. 2.3. The reduction of the number of VE by Y reduces the sp^3d^2-hybridisation in the t_{2g}-like symmetry, whereas Nb and Ta strengthen the metallic bonding character by an additional *d*-electron, since COM_{met} shifts to lower values. The substitution of Ti by isovalent Hf atoms has thus no significant effect on the metallic bonding behaviour. For a detailed description, please see Publications IV, VII and VIII.

Due to the fact that in cubic alloys, six nearest nitrogen neighbours surround the metal (compare section 2.2), it is more suggestive to discuss the effect of the various binary TMN in a solid solution with $Ti_{1-x}Al_xN$. Therefore, some basic properties of the respective cubic binaries are schematically summarised in Fig. 3.8. Since, the incorporation of TM at the metal sublattice significantly changes the bonding character and thus also the lattice parameter of the alloy, the cubic lattice parameters, ac, of the binary TMN related to the reference coating of $Ti_{0.42}Al_{0.58}N$ can facilitate the understanding of stress/strain development with increasing TM-content.

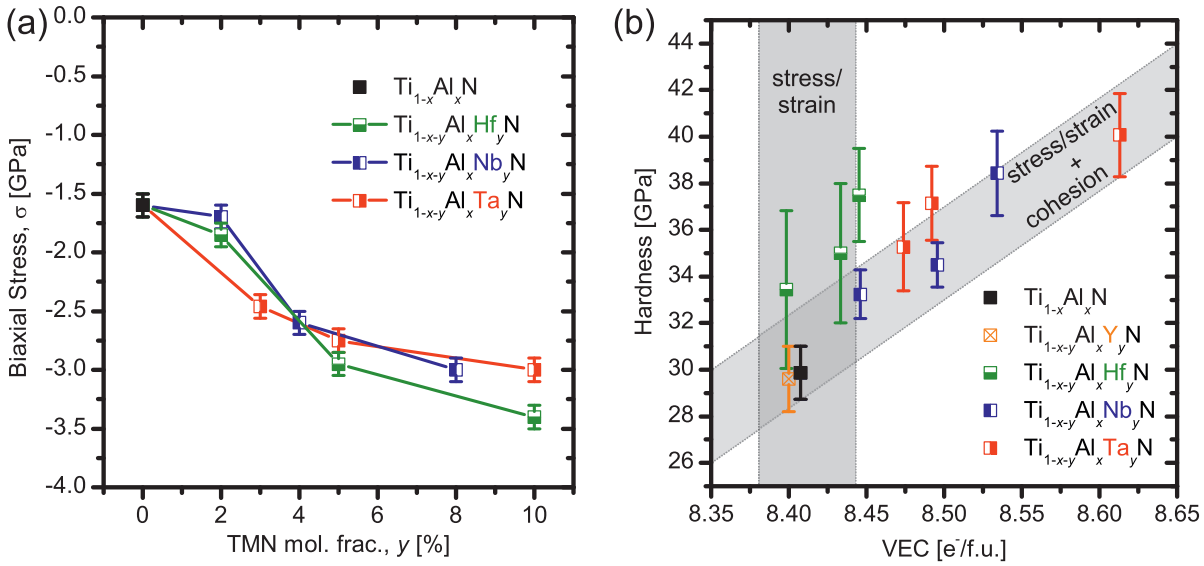

Figure 3.9: (a) Biaxial stress of the c-$Ti_{1-x-y}Al_xTM_yN$ films as a function of TMN content. (b) Film hardness of c-$Ti_{1-x-y}Al_xTM_yN$ films over the valence electron concentration, VEC. The solid solution hardening effect of Hf-alloying can be attributed mostly to lattice strain, while a VEC increase due to Nb- and Ta-substitution of Ti atoms promote the cohesive strength of the alloy, compare with Fig. 3.7.

The lattice parameter difference, Δa_c, of the TMN compared to $Ti_{0.42}Al_{0.58}N$ hence introduces significant strain in the quaternary $Ti_{1-x-y}Al_xTM_yN$ alloys. Consequently the compressive stresses, σ, of the $Ti_{1-x-y}Al_xTM_yN$ films increases steadily with increasing amount of TM, as shown in Fig. 3.9a. In addition, all quaternary films exhibit a positive deviation from Vegard's rule [161]. Moreover, the varying number of VE per formula unit results in a change of the total valence electron concentration, VEC, which provides a rough estimate for the hardness according to Holleck [20] who observed a hardness maximum at $VEC \approx 8.4$ for ternary TM-carbonitrides. By opposing the experimentally observed film hardness as a function of VEC, it is possible to discriminate the influence of TM-induced lattice strain or compressive stress and the changes of the electronic structure with respect to cohesion, as presented in Fig. 3.9b.

Since, Y (three VE) lowers the interatomic bonding strength by substitution of Ti (four VE) at the metallic sublattice, a reduction of VEC goes along with reduced hardness. Moreover, a sp^3 hybridisation of the wurtzite phase becomes more favourable for higher Y-contents, in agreement with the experimentally observed structural changes (see [156] and Publication IV). On the opposite, the introduction of five-valent Nb or Ta enhances the interatomic bonding strength, by promoting the interaction of the metal d-states with N p-states. This behaviour favours the sp^3d^2-hybridisation of the metallic region close to E_F (see Publication IV and VII), which results in increased cohesive strength of the quaternary alloy

compared to $Ti_{1-x}Al_xN$. The solid solution hardening effect of dissolved ZrN and HfN in $Ti_{1-x-y}Al_xTM_yN$ can however almost exclusively be related to Δa_c, since the incorporation of Zr and Hf exhibit almost no impact on the electronic structure of the alloy. Details can be found in Publications IV–VIII.

3.3.3 Thermal Stability of $Ti_{1-x-y}Al_xTM_yN$

In order to get an estimate for the driving force for isostructural decomposition of quaternary $6Ti_{1-x-y}Al_xTM_yN$ alloys, DFT calculations were used for the determination of the mixing enthalpy, H_{mix}, which resembles the development of the energy of formation, E_f (compare Fig. 3.6), respectively. Since all H_{mix} values of the quaternary alloys are positive, the total energy of the system will be lowered due to decomposition into the boundary phases. By examination of H_{mix} of the individual ternary boundary TMN alloys it is possible to predict the stable phases after decomposition, see Fig. 3.10.

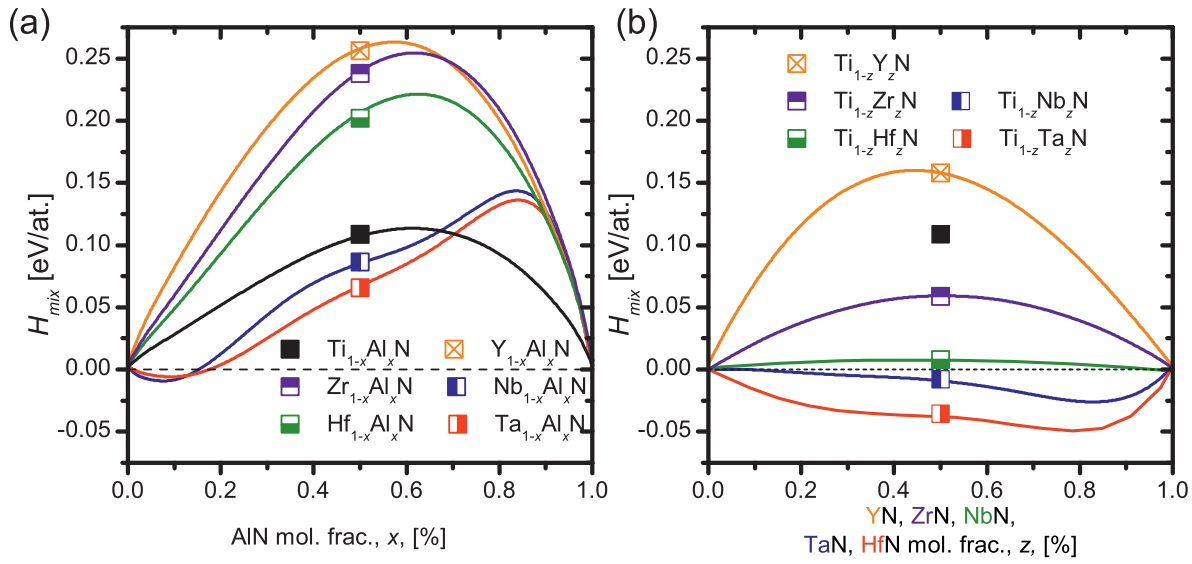

Figure 3.10: Mixing enthalpies, H_{mix}, of (a) $TM_{1-x}Al_xN$ and (b) $Ti_{1-z}TM_zN$ for a decomposition into the cubic boundary phases. Details are included in Ref. [24, 27] and Publications IV to VIII.

All ternary $TM_{1-x}Al_xN$ exhibit strongly positive H_{mix} with respect to c-TMN and c-AlN or w-AlN, which scale with the Al content and reach their maximum around the metastable solubility limit of the respective cubic ternary phase. From this it is possible to predict that after decomposition no ternary $TM_{1-x}Al_xN$ phase exists. Performing the same sort of calculation for the ternary $Ti_{1-z}TM_zN$, using $z = y/(1-x)$, the situation changes, as H_{mix}

is significantly lowered with respect to the metastable ternary $Ti_{1-x}Al_xN$ for TM-element additions of group IVB and VB.

For Nb and Ta additions, a solid solution of $Ti_{1-z}Nb_zN$ and $Ti_{1-z}Ta_zN$ is even more stable than the binary TMN throughout the whole composition range. A negligible driving force exists for $Ti_{1-z}Hf_zN$, while $Ti_{1-z}Zr_zN$ can be regarded as a border case, since it exhibits positive H_{mix} but only half the magnitude of $Ti_{1-x}Al_xN$. On the opposite, $Ti_{1-z}Y_zN$ exhibits an even higher driving force for decomposition, compared to $Ti_{1-x}Al_xN$, suggesting a strong driving force for phase separation into the binary c-TiN and c-YN [87].

These predictions are extremely helpful in order to determine the stability of the various possible phases forming in course of thermal load. As explained in section 3.2 spinodal decomposition into c-AlN- and c-TiN-rich domains causes age hardening of the ternary $Ti_{1-x}Al_xN$ system. Investigations on the structural evolution of c-$Ti_{1-x-y}Al_xTM_yN$ thin films as a function of Ta have proven that the initial stages of decomposition can be related to the spinodal formation of c-AlN-rich and c-Ti(TM)N-rich domains, before precipitation of w-AlN occurs and over-ageing causes decreasing film hardness.

The development of structure and the corresponding volume fractions is schematically shown in Fig. 3.11 for ternary c-$Ti_{1-x}Al_xN$ (a) and the quaternary c-$Ti_{1-x-y}Al_xTM_yN$ (b, c) alloys. In agreement with *ab initio* predictions the formation of a dual phase structure, consisting of w-AlN and a solid solution of c-$Ti_{1-z}TM_zN$, was observed after decomposition into the thermodynamically stable phases at high temperatures for all c-$Ti_{1-x-y}Al_xTM_yN$ alloys up to $y \approx 0.1$ (see Publications V to VIII and Refs. [87, 103, 136]). The only exception is c-$Ti_{1-x-y}Al_xY_yN$, which further decomposes into w-AlN, c-TiN and c-YN [87], as suggested from the interpretation of H_{mix} (see Fig. 3.11c).

The corresponding development of film hardness is shown in Fig. 3.11d. Although the extent of the hardness increase becomes less pronounced with increasing TM-content in the films, the hardness increase starts at lower T_a but is maintained to higher T_a (compare Figs. 3.11a and b). Since increasing isostatic pressure is known to promote the isostructural decomposition of $Ti_{1-x}Al_xN$, it is likely that TM-alloying similarly enhances the driving force for spinodal decomposition because of the increasing compressive stresses in the coatings with increasing amount of TM at the metallic sublattice (compare Fig. 2.6 in section 2.2). Hence, the hardness increases already at lower T_a. On the other hand, the higher coherency strain between the isostructurally formed phases, due to an increasing lattice mismatch between the c-AlN-rich and c-Ti(TM)N-rich domains imply a retarding force for the precipitation of w-AlN, which requires $\approx 24\%$ bigger volume per formula unit than c-AlN. Further details are given in Publications III, VI to VIII and Refs. [66, 74, 155].

By means of vacuum annealing treatments it is possible to determine e.g. temperature and

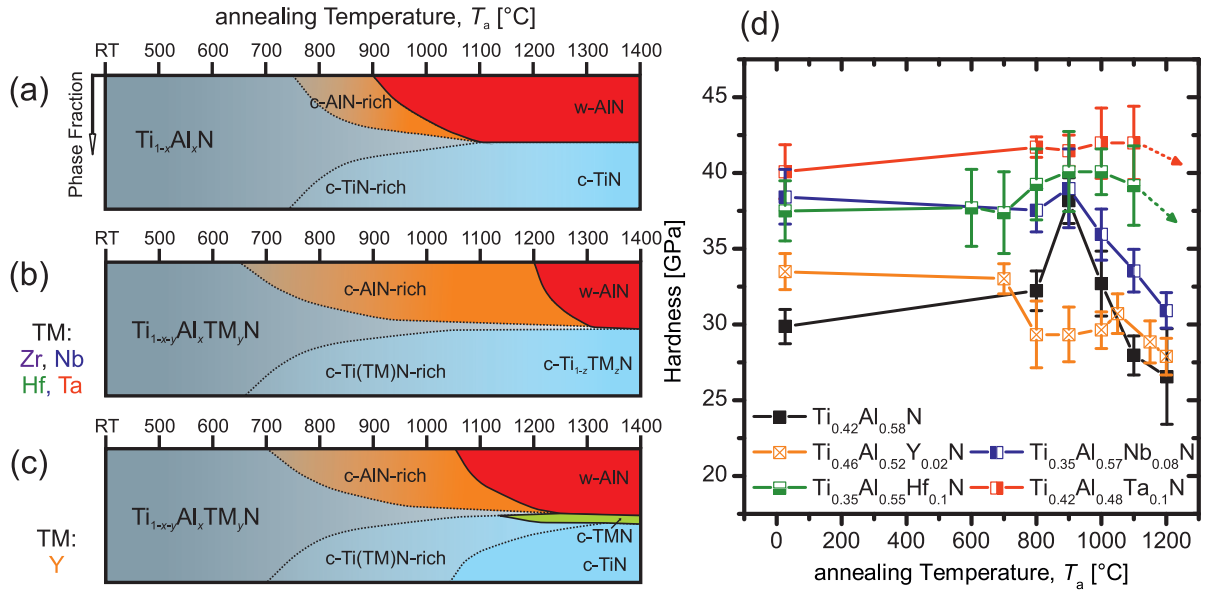

Figure 3.11: Schematic showing the structural evolution of metastable c-$Ti_{1-x}Al_xN$ as a function of T_a with corresponding phase fractions (a). The formation of c-AlN- and c-TiN-enriched domains during spinodal decomposition (see Publications II and III) is followed by the precipitation of w-AlN and deteriorating mechanical properties (d) in the final dual phase regime. The evolution of quaternary c-$Ti_{1-x-y}Al_xTM_yN$ alloys is shown for (b) the formation of dual phase structure (w-AlN + c-Ti(TM)N) at high temperatures in case of group IV and VB elements or (c) the formation of three stable phases after decomposition in case of Y alloyed $Ti_{1-x}Al_xN$.

mechanisms for the decomposition route of $Ti_{1-x-y}Al_xTM_yN$ under thermal load as discussed above. The observed structural evolution towards the predicted equilibrium phases is however only valid for dissociation in vacuum or protective gas atmosphere. In order to estimate the thermal stability of protective coatings, where high-temperature oxidation in ambient air is among the predominant failure mechanisms, additional annealing treatments were conducted at 850 and 950 °C (20 hours) under ambient atmosphere. The remaining nitride thickness of the $Ti_{1-x-y}Al_xTM_yN$ films on Al_2O_3, was determined from SEM cross-sections after thermal load and normalised to the as deposited thickness, as presented in Fig. 3.12. It can be seen that the ternary $Ti_{1-x}Al_xN$ suffers from complete oxidation, while all TM-alloyed films exhibit remaining nitride layers after oxidation at 850 °C (Fig. 3.12a). Already small TM-additions of 3 to 5 at.% at the metallic sublattice result in efficient oxidation protection in the case of TM = Zr, Nb, Hf, and Ta (compare to Refs. [103, 136] and Publications VII and VIII). Similar observations were achieved for thermal exposure at 950 °C, where however only the $Ti_{1-x-y}Al_xTM_yN$ films alloyed with Ta provided significantly improved oxidation resistance for little TM contents, whereas Nb and Hf only achieve

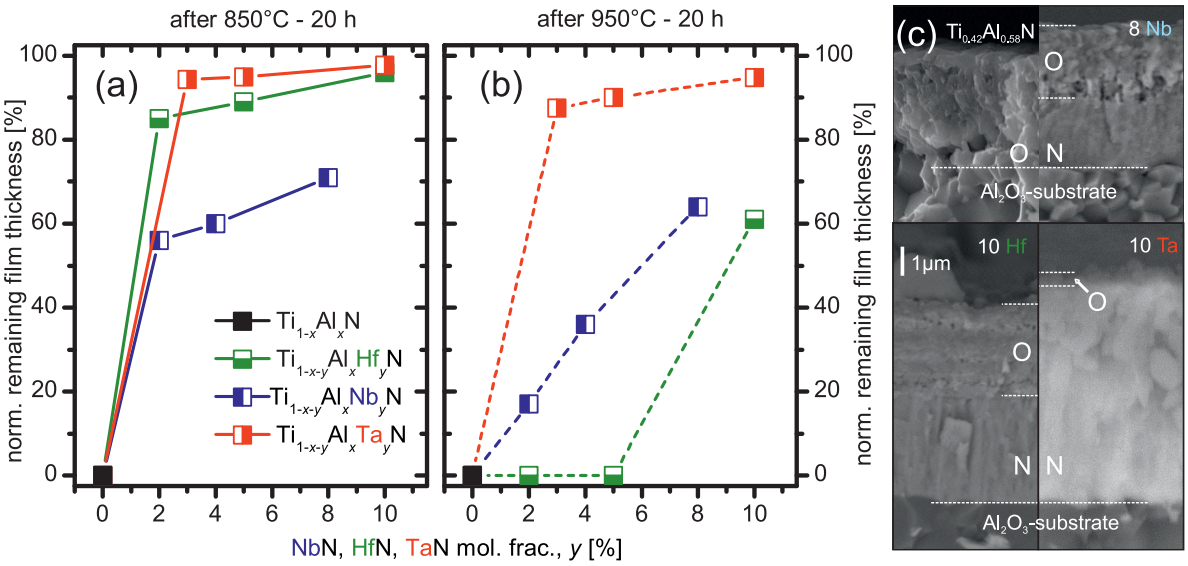

Figure 3.12: Unaffected nitride layer thicknesses of $Ti_{1-x-y}Al_xTM_yN$ films with TM = Hf, Nb and Ta after annealing in ambient air at (a) 850 °C and (b) 950 °C for 20 hours, with respect to the as deposited coating thickness. (c) Electron backscatter images of $Ti_{1-x-y}Al_xTM_yN$ fracture cross-sections. From top left to bottom right: the fully oxidised $Ti_{0.42}Al_{0.58}N$ film, and $Ti_{1-x-y}Al_xTM_yN$ from (b) with highest TM-contents investigated after annealing at 950 °C. The oxide scale is referred to as O and the remaining nitride as N, respectively. The best performance was achieved for the Ta-containing coating where only negligible oxidation occurred.

satisfying protection for $y \gtrapprox 8$ at.% (Fig.3.12b).

The growing oxide scale equally consists of a dense Al_2O_3-layer on top for all $Ti_{1-x-y}Al_xTM_yN$ films investigated (compare Figs. 3.13 and 3.14). This Al-rich oxide is known to reduce the oxygen indiffusion and only retains the coating lifetime if the porous Ti-rich oxide underneath does not suffer from mechanical load, which causes spallation of the brittle oxide scale [45]. In the case of the Zr- [103] and Hf-alloyed $Ti_{1-x-y}Al_xTM_yN$ films an alternating layer structure develops, which consists of Al- and Ti-enriched oxides (see Fig. 3.13).

The respective TM remains with Ti, forming a mixed Ti-TM-oxide, as indicated by the EDX-element maps, where a slight oxygen depletion in the Ti-rich domains compared to the Al-rich scale can be identified. The effective enhancement of the Zr- and Hf-alloyed films can thus be attributed to the higher activation energy for diffusion of the TM compared to Ti or Al [162]. Further details are included in Publication VIII.

On the other hand, the incorporation of Nb and Ta in $Ti_{1-x-y}Al_xTM_yN$ exhibits an even more effective protection against oxidation even after a thermal load of 950 °C for 20 hours (compare Fig. 3.12 and Fig. 3.14). Akin to the TM-elements of group IVB (Zr, Hf), a higher

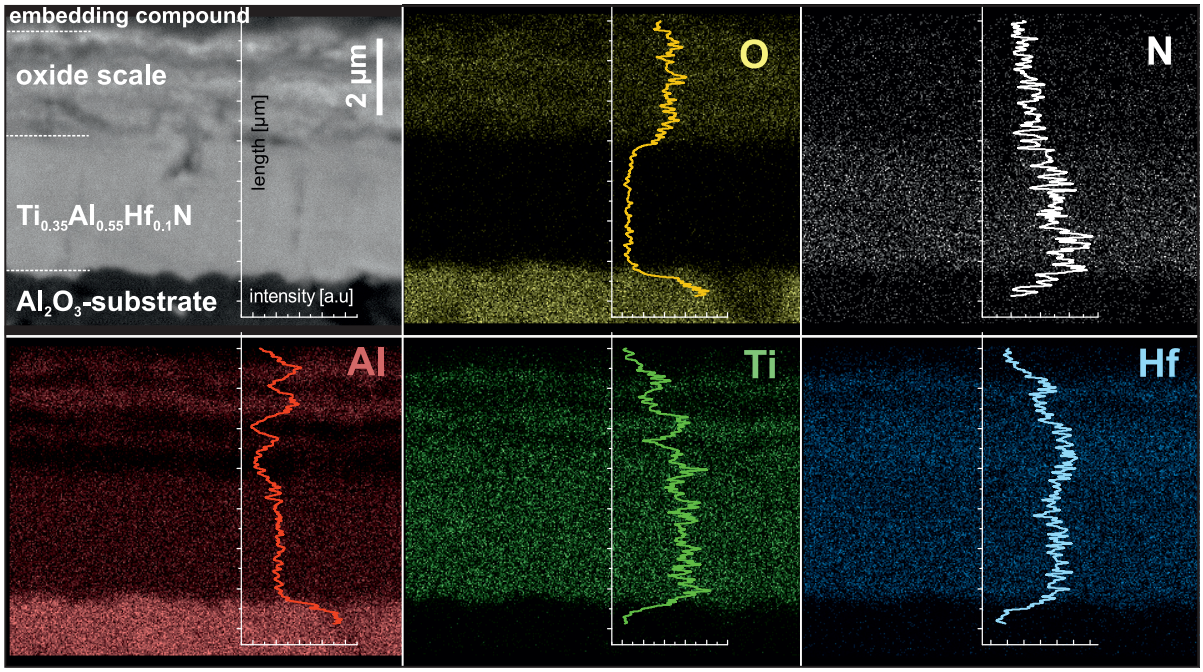

Figure 3.13: EDX elemental map of a $Ti_{0.35}Al_{0.55}Hf_{0.1}N$ cross-section after annealing at 950 °C for 20 hours. A self-organised multilayer of Al_2O_3 and a mixed Ti–Hf-oxide has formed on top of the unaffected nitride layer.

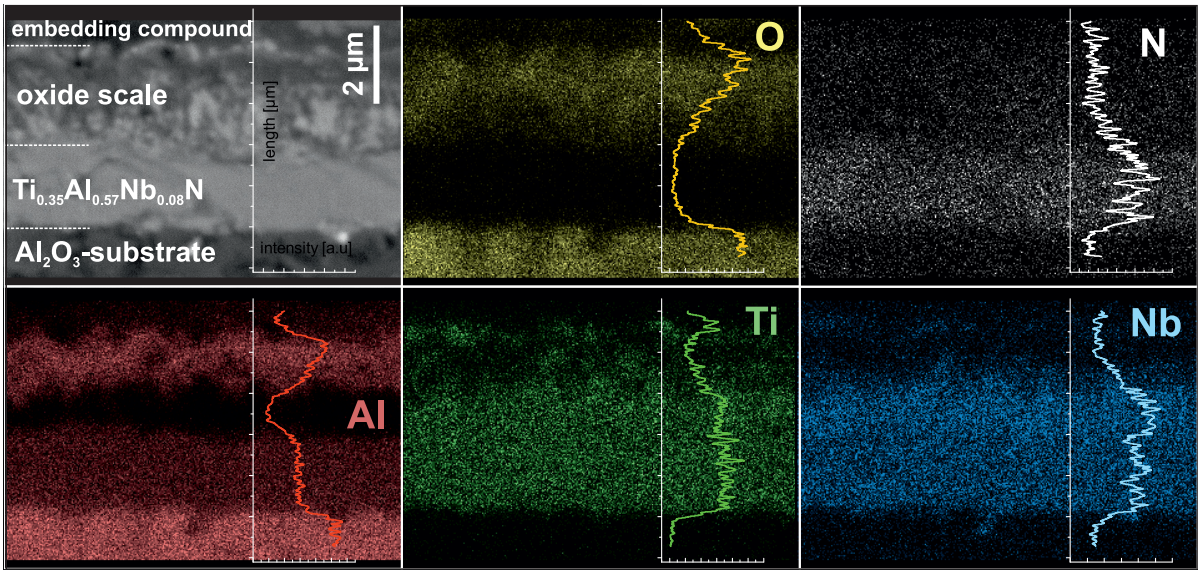

Figure 3.14: EDX elemental map of a $Ti_{0.35}Al_{0.57}Nb_{0.08}N$ cross-section after annealing at 950 °C for 20 hours. A dense Al_2O_3 top layer and a porous mixed Ti–Nb-oxide near the interface can clearly be distinguished (compare Fig. 3.12c).

activation energy of Nb or Ta results in a dense Al-rich top layer and an Ti(Nb)- or Ti(Ta)-enriched layers below. The different diffusion kinetics are also assumed to account for the higher porosity at the interface of the Ti-Nb-oxide and the virgin coating (see Fig. 3.12c). In addition, the substitution of Ti^{3+} ions by Nb^{5+} or Ta^{5+} ions is meant to effectively slow down the oxygen anion indiffusion, due to a reduction of oxygen vacancies. Further details can be found in Ref. [101, 163] and Publication VII.

Chapter 4

Summary of Publications and Contribution to the Field

Publication I:

A focused ion beam (FIB) microscopy-based lift-out technique was modified in order to fulfil the specific requirements for atom probe tomography (APT) of thermally treated transition-metal nitride (TMN) thin films. The method includes information on the set up and parameters for APT of free-standing low-conductivity TMN-coating material and the interplay between attached coating specimen and different support materials (low-carbon steel and doped silicon) during laser-assisted APT. In this work, the suitability of APT for the detection of impurities has been investigated in terms of the oxygen impurity distribution in thermally treated $Ti_{0.46}Al_{0.54}N$ thin films. Further, the given information enables for analysis of morphological and chemical features along the cross-section of thin films, which effectively enhances the possibility to cross several grain boundaries in case of thin films with columnar structure, in contrast to traditional preparation techniques.

Publication II:

The isostructural decomposition of cubic (fcc, B1-structure, $Fm\overline{3}m$ space group, NaCl-prototype) $Ti_{0.46}Al_{0.54}N$ thin films has been investigated by laser-assisted APT. Small initial chemical fluctuations at the metallic sublattice of $Ti_{0.46}Al_{0.54}N$ thin films were detected already after deposition. Free-standing $Ti_{0.46}Al_{0.54}N$ thin films investigated after annealing to 900 °C for 1 min, exhibited a three-dimensional interconnected structure of cubic TiN-rich ($Ti_{1-x+\Delta}Al_{x-\Delta}N$) and AlN-rich ($Ti_{1-x-\Delta}Al_{x+\Delta}N$) domains. The observed morphological features, such as the increasing deviation from the average chemical composition of the films

and the diffuse domain boundaries between the respective TiN- and AlN-enriched domains, clearly indicate uphill diffusion and thus spinodal decomposition as the underlying mechanism. The ongoing phase separation into the thermodynamically stable cubic TiN and wurtzite (B4-structure, $P6_3mc$ space group, ZnS-prototype) AlN was shown by investigation of $Ti_{0.46}Al_{0.54}N$ thin films after annealing to 1350 °C. This report is subject to the first successful application of laser-assisted APT for the study of phase separation in transition metal nitride hard coatings.

Publication III:

A combined approach, including X-ray diffraction (XRD), high-resolution transmission electron microscopy (HR-TEM), nanoindentation, four-point probe measurements, laser-assisted APT and DFT calculations, was used in order to solve a long standing question on the interplay of temperature and time during spinodal decomposition of c-$Ti_{1-x}Al_xN$ thin films. The microstructural evolution of c-$Ti_{0.46}Al_{0.54}N$, which exhibits a high driving force for isostructural decomposition, was associated with mechanical and electrical properties during vacuum annealing up to 1400 °C. A detailed description of the decomposition pathway of c-$Ti_{0.46}Al_{0.54}N$ exploits the importance and development of coherency strains on the age hardening effect of $Ti_{1-x}Al_xN$. The steady increase of the microstructural strain, ε, within the single phase cubic regime up to annealing temperatures of 1000 °C (for an annealing time, t_a, of 1 min) and 800 °C (t_a = 120 min) can be attributed to spinodal decomposition and the formation of coherent cubic TiN- and AlN-enriched domains, which results in peak hardness at the respective temperatures (and corresponding t_a). Increasing the annealing temperature (e.g. > 1000 °C for t_a = 1 min) or time (e.g. 120 min at 900 °C) enable for the phase transformation of the metastable c-AlN-rich domains towards the stable w-AlN, which first causes a dramatic strain increase (due to the higher specific volume of w-AlN) but yield no further hardness increase. With growth of w-AlN the development of a dual phase structure goes along with loss of coherency between the phases, reduction of ε and decreasing film hardness.

Publication IV:

The transition metal (TM) alloying effect of Y and Nb on the development of microstructure and mechanical properties of $Ti_{1-x}Al_xN$ thin films was studied. *Ab initio* calculations are used to exploit the structural transition from cubic to wurtzite structure in the case of $Ti_{1-x-y}Al_xY_yN$ for Y contents $\gtrapprox$ 5 at.% at the metal sublattice. The Y incorporation induces a decreasing grain size but also decreasing film hardness, in contrast to a classical Hall-Petch [164] relationship. An opposite behaviour was found for Nb alloying, where the

microstructural feature size increased but also an increasing hardness was observed up to the highest Nb additions of 8 at.% at the metal sublattice. The reason for this behaviour was identified by density functional theory, which allowed for the calculation of the different alloying effects of group IIIB (Y) and VB (Nb) TM-elements. Analysis of the density of states have shown, that change of the electronic structure either results in a preferred sp^3 hybridisation and thus the transition of cubic $Ti_{1-x-y}Al_xTM_yN$ towards the wurtzite modification (in case of Y alloying) or an enhanced d–d orbital interaction (for Nb alloying) while keeping the sp^3d^2 hybridisation, which strengthens the bonding in $Ti_{1-x-y}Al_xNb_yN$.

Publication V:

The impact of Nb alloying on structure and phase stability of $Ti_{1-x}Al_xN$ thin films, deposited by magnetron sputtering from Ti-Al-Nb targets with two different Ti/Al ratios of 1:1 and 1:2 and increasing Nb contents of 0, 2, 4, 8 and 0, 2, 5, and 10 at.%, respectively, was investigated in the as deposited state and after vacuum annealing to 1450 °C. The experimental findings from XRD after deposition support the *ab initio* calculations on the cubic metasolubility limit in $Ti_{1-x-y}Al_xNb_yN$ alloys, which only slightly shifts from $x \approx 0.69$ to ≈ 0.68 for Nb additions of $y = 0$ and 0.125, respectively. The higher Al containing $Ti_{1-x-y}Al_xNb_yN$ coatings exhibit either a single phase wurtzite or a dual phase (cubic/wurtzite, c/w) structure. Comparison of the *ab initio* obtained data and experiments, in terms of calculated lattice constants and the observed phases after decomposition due to the annealing treatment, yield a good agreement. It is shown, that supersaturated c-$Ti_{1-x-y}Al_xNb_yN$ films fully decompose into a solid solution of c-$Ti_{1-z}Nb_zN$ (with $z = y/(1-x)$ and w-AlN during annealing to 1450 °C, while the w- and c/w-$Ti_{1-x-y}Al_xNb_yN$ films exhibit a tendency for further precipitation of Nb–N phases.

Publication VI:

Density functional theory calculations were employed to predict the thermodynamically stable compounds, forming from a supersaturated solid solution of c-$Ti_{1-x-y}Al_xTa_yN$ thin films in course of vacuum annealing to 1400 °C. The *ab initio* predicted positive deviation of the cubic lattice parameters (a_c) for $Ti_{1-x-y}Al_xTa_yN$ alloys (with $y = 0$, 0.056 and 0.11) from a linear interpolation (Vegard's rule) of a_c of the binary boundary systems is experimentally proven by X-ray diffraction measurements of powdered as deposited $Ti_{1-x-y}Al_xTa_yN$ thin films with increasing Ta content of 0, 3, 5, and 10 at.% at the metallic sublattice, respectively. The difference in a_c between DFT calculation and experiment is within $\approx 1\%$. Further, a methodical approach is presented which uses the mixing enthalpies, H_{mix}, of the ternary boundary phases of $Ti_{1-x-y}Al_xTa_yN$ to estimate the formation of the thermodynamically

stable phases after decomposition. The theoretical approach predicts a dual phase structure of wurtzite AlN and a solid solution of cubic $Ti_{1-z}Ta_zN$, with $z = y/(1-x)$, after decomposition. A positive H_{mix}, as calculated for $Ti_{1-x}Al_xN$ and $Al_{1-y}Ta_yN$ throughout the whole composition range, indicates a high driving force for decomposition while on the opposite the negative H_{mix} of $Ti_{1-y}Ta_yN$ points towards a more stable phase. These results are confirmed by XRD measurements on the vacuum annealed $Ti_{1-x-y}Al_xTa_yN$ films and demonstrate that *ab initio* calculated H_{mix} can be used to accurately predict thermodynamical phase stability of quaternary solid solutions.

Publication VII:

The electronic structure of the c-$Ti_{1-x-y}Al_xTa_yN$ alloy compositions discussed in Publication VI, is analysed with the goal to estimate the thermal stability of the quaternary thin films. The *ab initio* results indicate a decreasing energy of formation, E_f, as well as increasing cohesive energies, E_{coh}, due to increased *d–d* orbital interaction (compare Publication IV) with increasing amount of Ta in the coatings. In order to determine the impact of Ta alloying on the thermal stability of c-$Ti_{1-x-y}Al_xTa_yN$, the coatings were exposed in vacuum to different annealing temperatures (T_a = 500 to 1400 °C in 100 °C steps) and times (t_a = 1, 120, and 480 min constant T_a = 900 °C). The experimental results indicate an akin decomposition route as observed for the cubic ternary $Ti_{1-x}Al_xN$ (compare Publications I–III), resulting in *age hardening* of the $Ti_{1-x-y}Al_xTa_yN$ films with increasing T_a. However, the appearance of w-AlN, usually going in line with decreasing film hardness, is effectively retarded to ≈ 200–300 °C higher Ta (or longer t_a at constant T_a of 900 °C), compared to the Ta free coatings. The formation of a dual phase structure of c-$Ti_{1-z}Ta_zN$ and w-AlN, initiated by spinodal decomposition, thus enhances the mechanical properties at high temperatures. Additional oxidation experiments performed at T_a = 850 and 950 °C for 20 hours corroborate the assumption that Ta alloying of $Ti_{1-x}Al_xN$ essentially increases the thermal stability of the coatings. Already Ta additions of 3 at.% to the metallic sublattice increase the remaining nitride thickness (with respect to the initial film thickness) of the $Ti_{1-x-y}Al_xTa_yN$ coatings from zero (Ta free $Ti_{0.41}Al_{0.59}N$) to ≈ 95 and ≈ 87% for T_a = 850 and 950 °C, respectively.

Publication VIII:

The cubic (meta)stability limit of $Ti_{1-x-y}Al_xHf_yN$ films has been experimentally checked as a function of Al content, x, and for Hf additions, y, up to 10 at.% at the metallic sublattice. A direct interpolation of the *ab initio* predicted solubility limits between the quasibinary TiN–AlN and HfN–AlN border cases, yield a good agreement with the experimental results of the various $Ti_{1-x-y}Al_xHf_yN$ films deposited on silicon single crystals and also literature reports.

Four selected compositions close to the metastable cubic solubility limit, e.g. $Ti_{0.41}Al_{0.59}N$, $Ti_{0.38}Al_{0.60}Hf_{0.02}N$, $Ti_{0.38}Al_{0.57}Hf_{0.05}N$, and $Ti_{0.35}Al_{0.55}Hf_{0.10}N$, have been selected for annealing treatments in vacuum and ambient air in order to estimate the impact of Hf on the thermal stability of $Ti_{1-x}Al_xN$. The increasing hardness with increasing amount on Hf in the coatings mainly stems from a size dependent strain hardening effect, rather than changes in the electronic structure (compare Publications IV and VII). With increasing Hf amount at the metallic sublattice of the $Ti_{1-x-y}Al_xHf_yN$ films, T_a where w-AlN can first be detected increases from $\approx 900\,^{\circ}C$ for $Ti_{0.41}Al_{0.59}N$ to $\approx 1100\,^{\circ}C$ for $Ti_{0.38}Al_{0.57}Hf_{0.05}N$. The corresponding peak hardness values of $\approx 38\,GPa$ ($y = 0$) and $\approx 40\,GPa$ ($y = 0.05$) are observed after vacuum annealing to $T_a = 900$ and $1000\,^{\circ}C$, respectively. The earlier hardness increase (at lower T_a) with increasing amount of Hf in the films can be attributed to the higher intrinsic stresses of the films, which promote the isostructural decomposition but retard the formation of w-AlN, akin to the $Ti_{1-x-y}Al_xTa_yN$ films investigated in Publication VII. Also an increased oxidation resistance with increasing Hf content in the films is observed for annealing in ambient air at $T_a = 850\,^{\circ}C$ for 20 hours, where the Hf free coatings suffer from complete oxidation. Increasing T_a by $100\,^{\circ}C$ to $950\,^{\circ}C$, results in fully oxidised films except the $Ti_{1-x-y}Al_xHf_yN$ coatings with $y = 0.1$, where a remaining nitride layer of $\approx 61\%$ with respect to the initial coating thickness can be observed.

Concluding Remarks:

The experimental studies of Publications I–III, employing a combination of 3D-APT, HR-TEM, XRD, and nanoindentation, enable for a comprehensive understanding of the *age hardening* phenomenon of cubic (c) $Ti_{1-x}Al_xN$ at the atomic scale. Based on these investigations, it has been necessary to define the most important factors accounting for the thermal stability of c-$Ti_{1-x}Al_xN$. It is shown that the formation of coherency strains between the isostructurally decomposing domains, e.g. c-$Ti_{1-x+\Delta}Al_{x-\Delta}N$ and c-$Ti_{1-x-\Delta}Al_{x+\Delta}N$, respectively, is crucial for the observed increase of the film hardness with increasing annealing temperature and/or time.

The goal to enhance the thermal stability of the ternary $Ti_{1-x}Al_xN$ films was persecuted by researching sophisticated transition metal (TM) alloying concepts in order to trigger the onset of the wurtzite (w) AlN phase-formation, which is known to result in deteriorating mechanical properties at high temperatures.

In this work, quantum mechanical calculations were utilised as a predictive trend-giver for the various alloying effects of group IIIB to VB transition metals (e.g. Y, Nb, Hf and Ta), and compared to experiments. It is shown that density functional theory (DFT) calculations can be employed to estimate e.g. phase stabilities of the various supersaturated $Ti_{1-x-y}Al_xTM_yN$

solid solutions after deposition, see for instance Publications IV and V, but also to predict the thermodynamically stable products after thermally activated decomposition as shown in Publications VI to VIII.

The good agreement between *ab initio* predictions and the observed properties of the quaternary $Ti_{1-x-y}Al_xTM_yN$ thin films indicates the strong correlation of the electronic structure in this class of nanostructured materials. Consequently, this work provides a significant contribution to the field of theory guided materials design, as it presents numerous examples for successful implementation of quantum mechanical calculations to the development of hard coatings with superior high-temperature properties.

Bibliography

[1] E. Arzt, Acta Mater. **46**, 5611 (1998).

[2] G. Dehm, Prog. Mater. Sci. **6**, 664 (2009).

[3] S. Veprek, A. S. Argon, and R. F. Zhang, Philos. Mag. **31–32**, 4104 (2010).

[4] J. Greene, *Handbook of Crystal Growth* (Elsevier Science Publishers, 1993).

[5] L. Hultman, Vacuum **57**, 1 (2000).

[6] C. Mitterer, P. Mayrhofer, and J. Musil, Vacuum **71**, 279 (2003).

[7] P. H. Mayrhofer, C. Mitterer, L. Hultman, and H. Clemens, Prog. Mater. Sci. **51**, 1032 (2006).

[8] M. Stueber, H. Holleck, H. Leiste, K. Seemann, S. Ulrich, and C. Ziebert, J. Alloys Compd. **483**, 321 (2009).

[9] K. Schwarz, P. Blaha, and S. B. Trickey, Mol. Phys. **108**, 3147 (2010).

[10] P. H. Mayrhofer, C. Mitterer, and H. Clemens, Adv. Eng. Mater. **7**, 1071 (2005).

[11] A. Carvaleiro, B. Trinidade, M. T. Vieira, and D. J. Lockwood, "The Influence of the Addition of a Third Element on the Structure and Mechanical Properties of Transition-Metal-Based Nanostructured Hard Films: Part I - Nitrides," in *Nanostructured Coatings*, edited by A. Cavaleiro and J. T. M. De Hosson (Springer Science+Business Media, LLC, New York, 2006).

[12] G. Dehm, C. Motz, C. Scheu, H. Clemens, P. H. Mayrhofer, and C. Mitterer, Adv. Eng. Mater. **8**, 1033 (2006).

[13] D. M. Mattox, *Handbook of Physical Vapor Deposition (PVD) Processing* (Noyes Publications, Westwood, New Jersey, 1998) p. 944.

[14] M. Ohring, *Materials Science of Thin Films* (Elsevier, Singapore, 2006).

[15] B. A. Movchan and A. V. Demchish, Phys. Met. Metallogr. **28**, 83 (1969).

[16] J. A. Thornton, J. Vac. Sci. Technol. **11**, 666 (1974).

[17] P. B. Barna and M. Adamik, Thin Solid Films **317**, 27 (1998).

[18] A. Anders, Thin Solid Films **518**, 4087 (2010).

[19] L. E. Toth, *Transition Metal Carbides and Nitrides* (Academic Press, New York, 1971).

[20] H. Holleck, J. Vac. Sci. Technol. A **4**, 2661 (1986).

[21] B. Eck, R. Dronskowski, M. Takahashi, and S. Kikkawa, J. Mater. Chem. **9**, 1527 (1999).

[22] E. Zhao and Z. Wu, J. Solid State Chem. **181**, 2814 (2008).

[23] G. M. Matenoglou, L. E. Koutsokeras, C. E. Lekka, G. Abadias, C. Kosmidis, G. A. Evangelakis, and P. Patsalas, Surf. Coat. Technol. **204**, 911 (2009).

[24] D. Holec, R. Franz, P. H. Mayrhofer, and C. Mitterer, J. Phys. D: Appl. Phys. **43** (2010).

[25] C. Stampfl and A. J. Freeman, Phys. Rev. B **71**, 24111 (2005).

[26] H. Holleck, Surf. Coat. Technol. **43-44**, 245 (1990).

[27] F. Rovere, *Materials Chemistry*, 1st ed. (Shaker Verlag GmbH, Aachen, 2010) p. 224.

[28] C. Stampfl, W. Mannstadt, R. Asahi, and A. J. Freeman, Phys. Rev. B **63**, 1551061 (2001).

[29] P. Fallböhmer, C. A. Rodriguez, T. Özel, and T. Altan, J. Mater. Process. Tech. **98**, 104 (2000).

[30] W. D. Münz, J. Vac. Sci. Technol. A **4**, 2717 (1986).

[31] H. Holleck and V. Schier, Surf. Coat. Technol. **76-77**, 328 (1995).

[32] P. C. Yashar and W. D. Sproul, Vacuum **55**, 179 (1999).

[33] P. Panjan, M. Cekada, and B. Navinsek, Surf. Coat. Technol. **174-175**, 55 (2003).

[34] P. H. Mayrhofer, P. E. Hovsepian, C. Mitterer, and W. D. Münz, Surf. Coat. Technol. **177-178**, 341 (2004).

[35] S. Veprek and S. Reiprich, Thin Solid Films **268**, 64 (1995).

[36] S. Veprek, J. Vac .Sci. Technol. A **17**, 2401 (1999).

[37] J. Musil and H. Hrubý, Thin Solid Films **365**, 104 (2000).

[38] H. Holleck, M. Lahres, and P. Woll, Surf. Coat. Technol. **41**, 179 (1990).

[39] R. Manaila, A. Devenyi, D. Biro, L. David, P. B. Barna, and A. Kovacs, Surf. Coat. Technol. **151-152**, 21 (2002).

[40] S. PalDey and S. C. Deevi, Mater. Sci. Eng. A **342**, 58 (2003).

[41] G. Beensh-Marchwicka, L. Krol-Stepniewska, and W. Posadowski, Thin Solid Films **82**, 313 (1981).

[42] H. A. Jehn, S. Hofmann, V. E. Ruckborn, and W. D. Münz, J. Vac. Sci. Technol. A **4**, 2701 (1986).

[43] O. Knotek, W. Bosch, and T. Leyendecker, J. Vac. Sci. Technol. A **4**, 2695 (1986).

[44] H. A. Jehn, S. Hofmann, and W. D. Münz, Thin Solid Films **153**, 45 (1987).

[45] D. McIntyre, J. E. Greene, G. Hakansson, J. E. Sundgren, and W. D. Münz, J. Appl. Phys. **67**, 1542 (1990).

[46] H. Holleck, Surf. Coat. Technol. **36**, 151 (1988).

[47] R. Cremer, M. Witthaut, A. Von Richthofen, and D. Neuschütz, Fresenius' Journal of Analytical Chemistry **361**, 642 (1998).

[48] R. Cremer, M. Witthaut, and D. Neuschuetz, in *TMS Annual Meeting* (1998) pp. 249–258.

[49] H. Hasegawa, A. Kimura, and T. Suzuki, Surf. Coat. Technol. **132**, 76 (2000).

[50] K. Kutschej, P. H. Mayrhofer, M. Kathrein, P. Polcik, R. Tessadri, and C. Mitterer, Surf. Coat. Technol. **200**, 2358 (2005).

[51] D. Holec, R. Rachbauer, L. Chen, L. Wang, D. Luef, and P. H. Mayrhofer, Surf. Coat. Technol. **under review** (2011).

[52] P. Spencer, Int. J. Mater. Res. **92**, 1145 (2001).

[53] P. H. Mayrhofer, D. Music, and J. M. Schneider, J. Appl. Phys. **100**, 94906 (2006).

[54] T. I. Selinder, D. J. Miller, K. E. Gray, M. R. Sardela Jr, and L. Hultman, Vacuum **46**, 1401 (1995).

[55] M. Brizuela, A. Garcia-Luis, I. Braceras, J. I. Onate, J. C. Sanchez-Lopez, D. Martinez-Martinez, C. Lopez-Cartes, and A. Fernandez, Surf. Coat. Technol. **200**, 192 (2005).

[56] Y. Makino, M. Mori, S. Miyake, K. Saito, and K. Asami, Surf. Coat. Technol. **193**, 219 (2005).

[57] A. E. Reiter, V. H. Derflinger, B. Hanselmann, T. Bachmann, and B. Sartory, Surf. Coat. Technol. **200**, 2114 (2005).

[58] H. C. Barshilia, N. Selvakumar, B. Deepthi, and K. S. Rajam, Surf. Coat. Technol. **201**, 2193 (2006).

[59] H. Klostermann, H. Fietzke, T. Modes, and O. Zywitzki, Rev. Adv. Mater. Sci **15**, 33 (2007).

[60] H. C. Barshilia, B. Deepthi, K. S. Rajam, K. P. Bhatti, and S. Chaudhary, J. Mater. Res. **23**, 1258 (2008).

[61] S. H. Sheng, R. F. Zhang, and S. Veprek, Acta Mater. **56**, 968 (2008).

[62] S. Kolozsvari, P. Pesch, C. Ziebert, M. Stueber, and S. Ulrich, Plasma Processes Polym. **6**, S146 (2009).

[63] R. Franz, M. Lechthaler, C. Polzer, and C. Mitterer, Surf. Coat. Technol. **204**, 2447 (2010).

[64] P. H. Mayrhofer, F. D. Fischer, H. J. Böhm, C. Mitterer, and J. M. Schneider, Acta Mater. **55**, 1441 (2007).

[65] B. Alling, A. V. Ruban, A. Karimi, O. E. Peil, S. I. Simak, L. Hultman, and I. A. Abrikosov, Phys. Rev. B **75**, 45123 (2007).

[66] B. Alling, M. Odén, L. Hultman, and I. A. Abrikosov, Appl. Phys. Lett. **95**, 181906 (2009).

[67] P. H. Mayrhofer, D. Music, and J. M. Schneider, Appl. Phys. Lett. **88**, 71922 (2006).

[68] J. W. Cahn, Acta Metall. **9**, 795 (1961).

[69] A. D. Porter and K. E. Easterling, *Phase Transformations in Metals and Alloys* (Van Nostrand Reinhold (UK), 1981).

[70] J. W. Cahn and P. Haasen, *Mater. Sci. and Technol. - A Comprehensive Treatment*, edited by E. J. Kramer, Vol. 5 (VCH, New York, 1991).

[71] P. H. Mayrhofer, A. Hörling, L. Karlsson, J. Sjölen, T. Larsson, C. Mitterer, and L. Hultman, Appl. Phys. Lett. **83**, 2049 (2003).

[72] B. Alling, A. Karimi, and I. A. Abrikosov, Surf. Coat. Technol. **203**, 883 (2008).

[73] A. Hörling, L. Hultman, M. Oden, J. Sjölen, and L. Karlsson, J. Vac. Sci. Technol. A **20**, 1815 (2002).

[74] D. Holec, F. Rovere, P. H. Mayrhofer, and P. B. Barna, Scripta Mater. **62**, 349 (2010).

[75] P. H. Mayrhofer, L. Hultman, J. M. Schneider, P. Staron, and H. Clemens, Int. J. Mater. Res. **98**, 1054 (2007).

[76] D. Heim and R. Hochreiter, Surf. Coat. Technol. **98**, 1553 (1998).

[77] P. Holubra, M. Jilek, and M. Sima, Surf. Coat. Technol. **120-121**, 184 (1999).

[78] C. Rebholz, J. M. Schneider, A. A. Voevodin, J. Steinebrunner, C. Charitidis, S. Logothetidis, A. Leyland, and A. Matthews, Surf. Coat. Technol. **113**, 126 (1999).

[79] O. Durand-Drouhin, A. E. Santana, A. Karimi, V. H. Derflinger, and A. Schütze, Surf. Coat. Technol. **163-164**, 260 (2003).

[80] J. M. Lackner, W. Waldhauser, R. Ebner, R. J. Bakker, T. Schöberl, and B. Major, Thin Solid Films **468**, 125 (2004).

[81] M. Parlinska-Wojtan, A. Karimi, O. Coddet, T. Cselle, and M. Morstein, Surf. Coat. Technol. **188-189**, 344 (2004).

[82] M. Stueber, P. B. Barna, M. C. Simmonds, U. Albers, H. Leiste, C. Ziebert, H. Holleck, A. Kovacs, P. Hovsepian, and I. Gee, Thin Solid Films **493**, 104 (2005).

[83] A. Flink, J. M. Andersson, B. Alling, R. Daniel, J. Sjölen, L. Karlsson, and L. Hultman, Thin Solid Films **517**, 714 (2008).

[84] L. A. Donohue, I. J. Smith, W. D. Münz, I. Petrov, and J. E. Greene, Surf. Coat. Technol. **94-95**, 226 (1997).

[85] L. A. Donohue, D. B. Lewis, W. D. Münz, M. M. Stack, S. B. Lyon, H. W. Wang, and D. Rafaja, Vacuum **55**, 109 (1999).

[86] E. Pflüger, A. Schroer, P. Voumard, L. Donohue, and W. D. Münz, Surf. Coat. Technol. **115**, 17 (1999).

[87] M. Moser, D. Kiener, C. Scheu, and P. H. Mayrhofer, Materials **3**, 1573 (2010).

[88] O. Knotek, T. Leyendecker, and F. Jungblut, Thin Solid Films **153**, 83 (1987).

[89] K. Kutschej, P. H. Mayrhofer, M. Kathrein, P. Polcik, and C. Mitterer, Surf. Coat. Technol. **188-89**, 358 (2004).

[90] K. Kutschej, P. H. Mayrhofer, M. Kathrein, P. Polcik, and C. Mitterer, Surf. Coat. Technol. **200**, 1731 (2005).

[91] M. Pfeiler, K. Kutschej, M. Penoy, C. Michotte, C. Mitterer, and M. Kathrein, Surf. Coat. Technol. **202**, 1050 (2007).

[92] M. Pfeiler, K. Kutschej, M. Penoy, C. Michotte, C. Mitterer, and M. Kathrein, Int. J. Refract. Met. H. **27**, 502 (2009).

[93] G. Gassner, P. H. Mayrhofer, K. Kutschej, C. Mitterer, and M. Kathrein, Surf. Coat. Technol. **201**, 3335 (2006).

[94] T. Reeswinkel, D. G. Sangiovanni, V. Chirita, L. Hultman, and J. M. Schneider, Surf. Coat. Technol. **205**, 4821 (2011).

[95] O. Knotek, M. Böhmer, T. Leyendecker, and F. Jungblut, Mat. Sci. Eng. **105-106**, 481 (1988).

[96] L. A. Donohue, J. Cawley, J. S. Brooks, and W. D. Münz, Surf. Coat. Technol. **74-75**, 123 (1995).

[97] R. Cremer and D. Neuschütz, Surf. Coat. Technol. **146-147**, 229 (2001).

[98] K. Kutschej, N. Fateh, P. H. Mayrhofer, M. Kathrein, P. Polcik, and C. Mitterer, Surf. Coat. Technol. **200**, 113 (2005).

[99] C. Feng, S. Zhu, M. Li, L. Xin, and F. Wang, Surf. Coat. Technol. **202**, 3257 (2008).

[100] M. Pfeiler, G. A. Fontalvo, J. Wagner, K. Kutschej, M. Penoy, C. Michotte, C. Mitterer, and M. Kathrein, Tribol. Let. **30**, 91 (2008).

[101] M. Pfeiler, C. Scheu, H. Hutter, J. Schnöller, C. Michotte, C. Mitterer, and M. Kathrein, J. Vac. Sci. Technol, A **27**, 554 (2009).

[102] V. Braic, C. N. Zoita, M. Balaceanu, A. Kiss, A. Vladescu, A. Popescu, and M. Braic, Surf. Coat. Technol. **204**, 1925 (2010).

[103] L. Chen, D. Holec, Y. Du, and P. H. Mayrhofer, Thin Solid Films **519**, 5503 (2011).

[104] L. Hultman, H. T. G. Hentzell, J. E. Sundgren, B. O. Johansson, and U. Helmersson, Thin Solid Films **124**, 163 (1985).

[105] M. Beckers, N. Schell, R. M. S. Martins, A. Mücklich, and W. Möller, Appl. Phys. Lett. **89**, 74101 (2006).

[106] M. Beckers, N. Schell, R. M. S. Martins, A. Mücklich, W. Möller, and L. Hultman, J. Appl. Phys. **99**, 34902 (2006).

[107] E. W. Müller, Zeitschrift für Physik **131**, 136 (1951).

[108] M. K. Miller, A. Cerezo, M. G. Hetherington, and G. D. W. Smith, *Atom Probe Field Ion Microscopy* (Oxford University Press, New York, 1996).

[109] K. F. Russell, M. K. Miller, R. M. Ulfig, and T. Gribb, Ultramicroscopy **107**, 750 (2007).

[110] M. K. Miller, Mater. Charact. **44**, 11 (2000).

[111] A. Cerezo, M. Abraham, P. Clifton, H. Lane, D. J. Larson, A. K. Petford-Long, M. Thuvander, P. J. Warren, and G. D. W. Smith, Micron **32**, 731 (2001).

[112] J. M. Hyde, M. K. Miller, M. G. Hetherington, A. Cerezo, G. D. W. Smith, and C. M. Elliott, Acta Metall. Mater. **43**, 3403 (1995).

[113] J. M. Hyde, M. K. Miller, M. G. Hetherington, A. Cerezo, G. D. W. Smith, and C. M. Elliott, Acta Metall. Mater. **43**, 3415 (1995).

[114] M. K. Miller, J. M. Hyde, M. G. Hetherington, A. Cerezo, G. D. W. Smith, and C. M. Elliott, Acta Metall. Mater. **43**, 3385 (1995).

[115] M. K. Miller, *Atom Probe Tomography: Analysis at the atomic level* (Kluwer Academic/Plenum Publishers, New York, 2000) p. 239.

[116] M. K. Miller and R. G. Forbes, Mater. Charact. **60**, 461 (2009).

[117] D. R. Kingham, Surf. Sci. **116**, 273 (1982).

[118] G. L. Kellogg, J. Appl. Phys. **52**, 5320 (1981).

[119] A. Cerezo, P. H. Clifton, M. J. Galtrey, C. J. Humphreys, T. F. Kelly, D. J. Larson, S. Lozano-Perez, E. A. Marquis, R. A. Oliver, G. Sha, K. Thompson, M. Zandbergen, and R. L. Alvis, Mater. Today **10**, 36 (2007).

[120] S. Veprek, M. G. J. Veprek-Heijman, P. Karvankova, and J. Prochazka, Thin Solid Films **476**, 1 (2005).

[121] F. Tang, B. Gault, S. P. Ringera, and J. M. Cairney, Ultramicroscopy **110**, 836 (2010).

[122] F. Tang, B. Gault, S. P. Ringera, P. Martinc, A. Bendavidc, and J. M. Cairney, Scr. Mater. **63**, 192 (2010).

[123] B. Gault, F. Vurpillot, A. Vella, M. Gilbert, A. Menand, D. Blavette, and B. Deconihout, Rev. Sci. Instrum. **77**, 43705 (2006).

[124] D. N. Seidman, Ann. Rev. Mater. Res. **37**, 127 (2007).

[125] D. Blavette, T. A. Kassab, E. Cadel, A. Mackel, F. Vurpillot, M. Gilbert, O. Cojocaru, and B. Deconihout, Int. J. Mater. Res. **99**, 454 (2008).

[126] A. Shariq, S. Mutas, K. Wedderhoff, C. Klein, H. Hortenbach, S. Teichert, P. Kücher, and S. S. A. Gerstl, Ultramicroscopy **109**, 472 (2009).

[127] B. Gault, A. Menand, F. De Geuser, B. Deconihout, and R. Danoix, Appl. Phys. Lett. **88** (2006).

[128] T. E. Kelly, D. J. Larson, K. Thompson, R. L. Alvis, J. H. Bunton, J. D. Olson, and B. R. Gorman, Ann. Rev. Mater. Res. **37**, 681 (2007).

[129] IMAGO, "(IVAS)," (2010).

[130] M. K. Miller, K. F. Russell, K. Thompson, R. Alvis, and D. J. Larson, Microsc. Microanal. **13**, 428 (2007).

[131] K. Thompson, D. Lawrence, D. J. Larson, J. D. Olson, T. F. Kelly, and B. Gorman, Ultramicroscopy **107**, 131 (2007).

[132] D. J. Larson, D. T. Foord, A. K. Petford-Long, H. Liew, M. G. Blamire, A. Cerezo, and G. D. W. Smith, Ultramicroscopy **79**, 287 (1999).

[133] G. B. Thompson, M. K. Miller, and H. L. Fraser, Ultramicroscopy **100**, 25 (2004).

[134] M. K. Miller, K. F. Russell, and G. B. Thompson, Ultramicroscopy **102**, 287 (2005).

[135] D. J. Larson, A. K. Petford-Long, Y. Q. Ma, and A. Cerezo, Acta Mater. **52**, 2847 (2004).

[136] R. Rachbauer, unpublished results (2008).

[137] A. Flink, M. Beckers, J. Sjölen, T. Larsson, S. Braun, L. Karlsson, and L. Hultman, J. Mater. Res. **24**, 2483 (2009).

[138] J. H. Bunton, J. D. Olson, D. R. Lenz, and T. F. Kelly, Microsc. Microanal. **13**, 418 (2007).

[139] O. C. Hellman, J. A. Vandenbroucke, J. Rüsing, D. Isheim, and D. N. Seidman, Microsc. Microanal. **6**, 437 (2000).

[140] C. Capdevila, M. K. Miller, K. F. Russell, J. Chao, and J. L. Gonzalez-Carrasco, Mat. Sci. Eng. A **490**, 277 (2008).

[141] J. S. Langer, M. Bar-On, and H. D. Miller, Phys. Rev. A **11**, 1417 (1975).

[142] O. C. Hellman, J. B. Du Rivage, and D. N. Seidman, Ultramicroscopy **95**, 199 (2003).

[143] G. K. Williamson and W. H. Hall, Acta Metall. **1**, 22 (1953).

[144] W. C. Oliver and G. M. Pharr, J. Mater. Res. **7**, 1564 (1992).

[145] M. Odén, L. Rogström, A. Knutsson, M. R. Terner, P. Hedström, J. Almer, and J. Ilavsky, Appl. Phys. Lett. **94**, 53114 (2009).

[146] A. Knutsson, M. P. Johansson, P. O. A. Persson, L. Hultman, and M. Odén, Appl. Phys. Lett. **93**, 143110 (2008).

[147] D. Rafaja, C. Wüstefeld, C. Baehtz, V. Klemm, M. Dopita, M. Motylenko, C. Michotte, and M. Kathrein, Metall. Mater. Trans. A **42**, 559 (2011).

[148] G. Kresse and J. Furthmüller, Comp. Mater. Sci. **6**, 15 (1996).

[149] G. Kresse and J. Furthmüller, Phys. Rev. B **54**, 11169 (1996).

[150] P. Blaha, K. Schwarz, G. Madsen, D. Kvasnicka, and J. Luitz, "Wien2k, an improved and updated version of ab initio calculation package originally published by Blaha P., Sorantin P.I., Trickey S.B., Full-potential linearized augmentd plane wave programs for crystalline systems, Comput. Phys. Commun. 59 (1990) 399-415," (2000).

[151] G. Kresse and D. Joubert, Phys. Rev. B **59**, 1758 (1999).

[152] Y. Wang and J. P. Perdew, Phys. Rev. B **44**, 13298 (1991).

[153] S. H. Wei, L. G. Ferreira, J. E. Bernard, and A. Zunger, Phys. Rev. B **42**, 9622 (1990).

[154] D. Holec, *Multi-scale modelling of III-nitrides: Selected topics from dislocations to the electronic structure* (VDM Verlag Dr. Müller, Saarbrücken, 2010).

[155] D. Holec, R. Rachbauer, D. Kiener, P. D. Cherns, P. M. F. J. Costa, C. McAleese, P. H. Mayrhofer, and C. J. Humphreys, Phys. Rev. B **83**, 165122 (2011).

[156] M. Moser and P. H. Mayrhofer, Scripta Mater. **57**, 357 (2007).

[157] P. H. Mayrhofer, R. Rachbauer, and D. Holec, Scripta Mater. **63**, 807 (2010).

[158] B. Predel, *Landolt-Börnstein - Group IV - Physical Chemisty 5a: Ac-Au-Au-Zr*, Vol. 5a: Ac-Au- (Springer Verlag, Berlin, 1991).

[159] B. Predel, *Landolt-Börnstein - Group IV - Physical Chemisty*, Vol. 5d: Cr-Cs (Springer Verlag, Berlin, 1994).

[160] B. Predel, *Landolt-Börnstein - Group IV - Physical Chemisty*, Vol. 5h: Li-Mg (Springer Verlag, Berlin, 1997).

[161] L. Vegard, Zeitschrift für Physik **5**, 17 (1921).

[162] C. Feng, S. Zhu, M. Li, L. Xin, and F. Wang, Oxid. Met. **71**, 63 (2009).

[163] M. Peters and C. Leyens, eds., *Titan and Ti-alloys* (Wiley-VCH, New York, 2003).

[164] P. Haasen, *Physical Metallurgy*, third edit ed. (Cambridge University Press, Cambridge, 1996).

Chapter 5

Publications

5.1 Publications included into this Thesis and Author Contributions

Publication I

Atom probe specimen preparation and 3D interfacial study of Ti–Al–N thin films
R. Rachbauer, S. Massl, E. Stergar, P. Felfer, P.H. Mayrhofer
Surf. Coat. Technol. 204 (2010), p. 1811–1816.
doi:10.1016/j.surfcoat.2009.11.020

Author contributions
The author produced the films, planned and set up the APT experiments, evaluated the data and wrote the manuscript. FIB preparation was performed by S. Massl, the APT measurements were performed by E. Stergar. P. Felfer provided helpful discussions during specimen preparation and P.H. Mayrhofer helped during interpretation.

Publication II

Three-dimensional atom probe investigations of Ti–Al–N thin films
R. Rachbauer, E. Stergar, S. Massl, M. Moser, P.H. Mayrhofer
Scripta Mater. 61 (2009), p. 725–729.
doi:10.1016/j.scriptamat.2009.06.015

Author contributions
The author produced the films, planned and set up the individual experiments, evaluated the

data and wrote the manuscript. Specimen preparation by FIB was performed by S. Massl, the APT measurements were conducted by E. Stergar. M. Moser and P.H. Mayrhofer provided helpful discussions and proof read the manuscript.

Publication III

Decomposition pathways in age hardening of Ti–Al–N films
R. Rachbauer, S. Massl, E. Stergar, D. Holec, D. Kiener, J. Keckes, J. Patscheider, M. Stiefel, H. Leitner, P.H. Mayrhofer
J. Appl. Phys. 110 (2011), art. no. 023515.
doi:10.1063/1.3610451

Author contributions
The author deposited the films, planned the experiments and performed all annealing treatments and subsequent structural, mechanical and electrical measurements. R.R wrote the manuscript and was essentially supported by S. Massl and M. Stiefel (APT specimen preparation), E. Stergar (APT measurements), D. Kiener (HR-TEM), J. Keckes (XRD data evaluation), and D. Holec (DFT calculations). H. Leitner, J. Patscheider and P.H. Mayrhofer provided equipment and helpful support during interpretation.

Publication IV

Electronic origin of structure and mechanical properties in Y and Nb alloyed Ti–Al–N thin films
R. Rachbauer, D. Holec, M. Lattemann, L. Hultman, P.H. Mayrhofer
Int. J. Mater. Res. (formerly Z. Metallkd.) 102 (2011) 6, p. 735–742.
doi:10.3139/146.110520

Author contributions
The author prepared the films, conducted the experiments and wrote the manuscript. All DFT calculations were performed by D. Holec. M. Lattemann provided valuable support during TEM analysis of the films. L. Hultman and P.H. Mayrhofer contributed with helpful discussions.

Publication V

Influence of Nb on the phase stability of Ti–Al–N
P.H. Mayrhofer, **R. Rachbauer**, D. Holec

Scripta Mater. 63 (2010), p. 807–810.
doi:10.1016/j.scriptamat.2010.06.020

Author contributions
The author prepared the films, and conducted all experiments. DFT calculations were performed by D. Holec and P.H. Mayrhofer. P.H. Mayrhofer also wrote the manuscript.

Publication VI

Phase stability and decomposition products of Ti–Al–Ta–N thin films
R. Rachbauer, D. Holec, P.H. Mayrhofer
Appl. Phys. Lett. 97 (2010), art. no. 151901.
doi:10.1063/1.3495783

Author contributions
The author planned the investigations, deposited the films, conducted the experiments and wrote the manuscript. All DFT calculations were performed by D. Holec. P.H. Mayrhofer contributed with helpful discussions and interpretation.

Publication VII

Increased thermal stability of Ti–Al–N thin films by Ta alloying
R. Rachbauer, D. Holec, P.H. Mayrhofer
Surf. Coat. Technol. (2011), doi: 10.1016/j.surfcoat.2011.07.009, article in press.
doi:10.1016/j.surfcoat.2011.07.009

Author contributions
The author grew the films, performed the annealing treatments and subsequent investigations of structural and mechanical properties. R.R. also wrote the manuscript. The DFT calculations were performed by D. Holec. D. Holec and P.H. Mayrhofer helped with interpretation of the *ab initio* results.

Publication VIII

Effect of Hf on structure and age hardening of Ti–Al–N thin films
R. Rachbauer, A. Blutmager, D. Holec, P.H. Mayrhofer
Manuscript in final preparation.

Author contributions
The author planned and directed the experiments. The preparation of the films and vacuum

annealing treatments were performed by A. Blutmager as a part of his diploma thesis. Coating oxidation and data evaluation was performed by R.R., who also wrote the manuscript. All DFT calculations were performed by D. Holec. P.H. Mayrhofer contributed with helpful discussions.

5.2 Publications related but not included into this Thesis

Publication IX

Towards predictive modelling of near-edge structures in electron energy–loss spectra of AlN based ternary alloys
D. Holec, **R. Rachbauer**, D. Kiener, P.D. Cherns, P.M.F.J. Costa, C. McAleese, P.H. Mayrhofer, C.J. Humphreys
Phys. Rev. B, 83 (2011), art. no. 165122.
doi:10.1103/PhysRevB.83.165122

Publication X

Phase stability and alloy-related trends in Ti–Al–N, Zr–Al–N and Hf–Al–N systems from first principles
D. Holec, **R. Rachbauer**, L. Chen, L. Wang, D. Luef, P.H. Mayrhofer
Surf. Coat. Technol. (2011), under review.

5.3 (Co)Supervised Diploma Thesis

Diploma Thesis A

Influence of Hf on the Phase Stability and Age-hardening of Ti–Al–N Hard Coatings
Andreas Blutmager, finished in December 2010.

Diploma Thesis B

Impact of Al on Structure and mechanical properties of NbN and TaN
Zehua Zhang, finished in April 2011.

Diploma Thesis C

Influence of Al on Structure and mechanical properties of YN and HfN
Lan Wang, finished in June 2011.